Draft version October 27, 2025
Typeset using LaTeX **default** style in AASTeX7.0.1

Backmapping of the High- and Low-latitude Solar Wind under Multiple Heliospheric and Coronal Magnetic Field Configurations

Xinyi Ma,[1,2] Liping Yang,[1] Xueshang Feng,[1,3] Hui Tian,[4,1] Honghong Wu,[5] Fang Shen,[1,2] Wangning Zhang,[1,6] Mengxuan Ma,[1,2] Xiao Zhang,[1,2] and Ziwei Wang[3]

[1] *State Key Laboratory of Solar Activity and Space Weather, National Space Science Center, Chinese Academy of Sciences, Beijing 100190, People's Republic of China*

[2] *College of Earth and Planetary Sciences, University of Chinese Academy of Sciences, Beijing 100049, People's Republic of China*

[3] *Shenzhen Key Laboratory of Numerical Prediction for Space Storm, School of Aerospace, Harbin Institute of Technology, Shenzhen 518055, People's Republic of China*

[4] *School of Earth and Space Sciences, Peking University, 100871 Beijing, People's Republic of China*

[5] *School of Electronic Information, Wuhan University, 430072 Wuhan, People's Republic of China*

[6] *School of Geophysics and Information Technology, China University of Geosciences (Beijing), China*

ABSTRACT

Solar wind backmapping is a critical technique for analyzing the origin of the solar wind and space weather events by correlating in situ measurements with solar remote-sensing observations. This technique typically traces magnetic field lines using a heliospheric magnetic field (HMF) model coupled with a coronal magnetic field (CMF). However, the impact of different HMF and CMF configurations on backmapping uncentainty-particularly regarding high-latitude solar wind-remains inadequately quantified. This study comprehensively evaluates solar wind backmapping by combining two HMF models (Parker spiral, Fisk-type) with three CMF models (Potential Field Source Surface (PFSS), Potential Field Current Sheet (PFCS), Current Sheet Source Surface (CSSS)). Our analysis primarily uses in situ measurements from Ulysses and remote-sensing data from STEREO-A. Key findings are that: (1) while both Fisk and Parker HMF models show comparable consistency with measured magnetic field strength and polarity, they produce certain longitudinal displacements in their back-mapped footpoints on the source surface ($2.5R_\odot$); (2) For CMF models (PFSS, PFCS, CSSS), predicted photospheric footpoints exhibit minor variations for high/mid-latitude solar wind but some divergences for ecliptic/low-latitude wind; (3) All three CMF models link high/mid-latitude wind to active regions or coronal holes, yet associate a fraction of ecliptic/low-latitude wind with quiet-Sun regions; (4) Ecliptic/low-latitude sources show significantly stronger dependence on the PFSS source surface height compared to high-latitude wind. These results demonstrate that simpler models (PFSS + Parker) appear reasonably adequate for polar coronal hole wind studies, while low-latitude/ecliptic solar wind exhibits the heightened sensitivity to model choices.

1. INTRODUCTION

Solar wind backmapping provides critical insights into solar-terrestrial physics, such as determining the origin of the solar wind, enabling space weather forecasting (M. Owens & R. Forsyth 2013; S. R. Cranmer 2025). Magnetic field configurations provide the essential topological linkage between dynamic solar phenomena and their manifestations in interplanetary space. By inversely tracing solar wind parcels measured in situ by spacecraft to their source locations on the solar surface, researchers can elucidate critical processes governing solar wind generation, acceleration, and heating mechanisms (J. Nolte & E. Roelof 1973; R. H. Levine et al. 1977; V. J. Pizzo 1981; M. Neugebauer et al. 1998; J. A. Linker et al. 1999; L. P. Yang et al. 2012; T. Peleikis et al. 2017; A. P. Rouillard et al. 2020; S. Parenti et al. 2021; S. D. Bale et al. 2023; P. Kumar et al. 2023; Y. J. Rivera et al. 2024; T. Ervin et al. 2024; C. Hou et al. 2024a,b; N. Bizien et al. 2025).

Corresponding author: Liping Yang, Xueshang Feng
lpyang@swl.ac.cn, fengx@spaceweather.ac.cn

Multiple methodologies facilitate magnetic connectivity across heliospheric domains. Some techniques extrapolate solar wind parameters near the Sun to a chosen heliospheric position, while others relate in situ measurements far from the Sun back to the solar atmosphere (P. Riley & R. Lionello 2011). Prominent methods include ballistic extrapolation (A. Balogh & G. Erdõs 2013), ad hoc kinetic mapping (C. N. Arge & V. J. Pizzo 2000), 1-D upwinding propagation (P. Riley & R. Lionello 2011), global magnetohydrodynamics (MHD) simulations (A. Posner et al. 2001), and so on. Among these, ballistic solar wind backmapping assumes the constant-speed radial flow of the solar wind and remains the most extensively utilized operational approach (A. Balogh & G. Erdõs 2013; M. Owens & R. Forsyth 2013; T. Peleikis et al. 2017; A. R. Macneil et al. 2021). This technique commonly combines the Potential Field Source Surface (PFSS) coronal magnetic field (CMF) model with the Parker spiral heliospheric magnetic field (HMF) model to trace in situ solar wind measurements inward to the solar disk.

The PFSS model assumes that the coronal magnetic field is potential and extrapolates the coronal magnetic structure from photospheric magnetic field observations. It further assumes the coronal field becomes radially open beyond a source surface, typically set at 2.5 solar radii (M. Altschuler & G. Newkirk 1969). The PFSS model is widely used to analyze coronal magnetic topology, study coronal large-scale structures, predict solar wind properties, and other applications (C. N. Arge & V. J. Pizzo 2000; R. Lin et al. 2024). However, it ignores the effect of electric currents (K. H. Schatten et al. 1969). To address this limitation, alternative CMF models like the Potential Field Current Sheet (PFCS) and Current Sheet Source Surface (CSSS) models have been developed. The PFCS model incorporates current sheets at magnetic polarity reversal sites, and can improves the directions and variations of magnetic fields to match remote sensing and in situ observations (K. H. Schatten 1971; G. Shi et al. 2024). The CSSS model accounts for horizontal coronal currents, producing notably smoother and more continuous open magnetic field lines than the PFSS model (X. Zhao & J. T. Hoeksema 1995; J. Koskela et al. 2019). These alternative CMF models can alter open-flux geometry, thereby modifying solar wind source mapping.

Beyond the source surface, solar wind backmapping relies on HMF models. The Parker spiral model is a widely used HMF approach, assuming magnetic fields are rooted at the Sun and carried outward by the steady, radial flow of the solar wind into interplanetary space (E. N. Parker 1958). This model describes how solar rotation twists magnetic fields into Archimedean spirals, which are confined to cones of constant heliographic latitude. When tracing solar wind measurements through the Parker spiral to the boundary of a CMF model, the ballistic approximation treats the solar wind with a constant speed, radial, plasma flow. Some studies enhance this approximation by incorporating solar wind acceleration and non-radial flow components (A. R. Macneil et al. 2021; J.-B. Dakeyo et al. 2024; X. Shi et al. 2024). These analyses reveal that solar wind acceleration and corotation effects counterbalance each other, which ultimately leads to a good performance of ballistic backmapping.

To explain recurrent energetic particle events observed at high latitudes by the Ulysses spacecraft, L. A. Fisk (1996) proposed an alternative to the Parker spiral HMF model that permits large excursions of magnetic fields in latitude. Based on a tilted magnetic dipole, the Fisk HMF model includes the interplay between footpoint differential rotation and magnetic field superradial expansion (T. H. Zurbuchen et al. 1997; L. A. Fisk et al. 1999; N. A. Schwadron & D. J. McComas 2003; R. A. Burger et al. 2008; P. J. Steyn & R. A. Burger 2020). To our knowledge, few studies have implemented the Fisk model in the solar wind backmapping, with P. J. Steyn et al. (2024) being the only application to traces field lines from L1 to the photosphere. Their results demonstrate exclusive mapping of the Fisk model to polar regions, contrasting with the PFSS model's mapping to equatorial and mid-latitude photospheric locations. By anchoring HMF footpoints in the photosphere and modeling their nonradial expansion through rigidly rotating coronal holes (predominantly polar), the Fisk model is particularly well-suited for tracing the fast solar wind back to its solar polar sources.

Despite widespread implementation, backmapping methodologies retain critical limitations. Ballistic backmapping is predominantly employed to relate ecliptic solar wind measurements with their coronal sources like mid-latitude coronal holes and active regions. However,it remains largely unexplored to connect back the high-latitude solar wind, which is typically associated with polar coronal holes. This knowledge gap is increasingly consequential given Solar Orbiter's out-of-ecliptic orbits (D. Müller et al. 2020) and China's planned solar polar-orbit observatory mission (Y. Deng et al. 2025). Furthermore, only the PFSS model and Parker models are widely implemented in backmapping studies. A rigorous evaluation of how different CMF and HMF models influence the identification of solar wind source region is warranted.

In this study, we employ the PFSS, PFCS, and CSSS CMF models alongside the Parker and Fisk HMF models to trace back solar wind measurements from Ulysses and Wind spacecraft to their solar origins. The resulting source locations are compared with Extreme Ultraviole Imagers (EUVI) observations from the Solar Terrestrial Relations Observatory Ahead spacecraft (STEREO-A). We quantify angular deviations between backmapping methods using different CMF/HMF model combinations, with particular focus on the fast solar wind originating from the Sun's polar regions. The paper is structured as follows: Section 2 details the observational data and the modeling frameworks. Section 3 presents and analyzes backmapping results across the CMF (PFSS, PFCS, CSSS) and HMF (Parker, Fisk) model configurations as well as different source surface heights of the PFSS model. Section 4 provides concluding remarks and discussion.

2. DATA AND MODELS

2.1. *In Situ Measurements*

As the first deep space probe to achieve a high-inclination orbit around the Sun, Ulysses completed the south pole crossing in early 2007 and arrived at the north pole at the end of the same year, conducting in situ measurements of the solar wind at latitudes $> 60°$. The magnetic field and plasma parameters were obtained by the Vector Helium Magnetometer (VHM) and Solar Wind Observations Over the Poles of the Sun (SWOOPS) (A. Balogh et al. 1992), respectively. In this work, we mainly use hour-averaged magnetic field and plasma data measured by the Ulysses spacecraft during its 2007 polar orbit, covering a heliocentric distance range of 1.4 to 2.3 AU and a latitude range from $80°S$ to $80°N$.

The Wind spacecraft locates at the L1 Lagrange point of the solar-terrestrial system, and continuously monitors the solar wind environment at upside of the earth. It records the temporal evolution of magnetic field, flow velocity, density and other parameters of the solar wind through the Magnetic Field Investigation (MFI) and the Solar Wind Experiment (SWE) (L. B. Wilson et al. 2021). In this work, we use hour-averaged magnetic field and plasma data measured by Wind spacecraft from September 10 to October 8, 2007 (J. H. King & N. E. Papitashvili 2020).

2.2. *Remote Sensing Observations*

Although promissing advances have been made recently in the measurements of the global coronal magnetic field (Z. Yang et al. 2020b,a, 2024), measurements of the 3D global magnetic field structure in the entire solar atmosphere are still not possible and we need to rely on the technique of magnetic field extrapolation. We utilize daily synoptic photospheric magnetograms generated by the Air Force Data Assimilative Photospheric Flux Transport (ADAPT) model (C. N. Arge et al. 2010) as the boundary condition for solar coronal magnetic field extrapolation. These ADAPT maps assimilate raw full-disk magnetograms obtained by the Global Oscillation Network Group (GONG). The GONG project maintains continuous solar monitoring through a global six-station network, synthesizing daily synoptic magnetograms (spatial resolution: 180 latitude $\times$ 360 longitude points in $\sin\theta$-ϕ coordinates). This multi-station strategy overcomes single-site limitations imposed by Earth's rotation and weather disruptions, enabling near-continuous photospheric magnetic coverage. Through ADAPT's flux transport physics, the assimilated maps provide dynamically consistent photospheric evolution of the magnetic field. In this work, we employs ADAPT maps covering seven CRs in 2007 and CR 2066 in 2008 to extrapolate coronal magnetic fields.

Additionally employed are observations of the lower corona obtained from the EUVI of the Sun Earth Connection Coronal and Heliospheric Investigation (SECCHI) suite onboard the STEREO-A spacecraft (R. A. Howard et al. 2008). EUVI observations can reveal coronal hole regions, active regions, quiet-Sun regions, and are thus applied to evaluate the accuracies of the mapped source regions of the solar wind (L. P. Yang et al. 2012; M. Owens & R. Forsyth 2013). In this work, we utilize synoptic maps derived from STEREO-A 195 $\mathring{A}$ full-disk EUVI observations. These maps were assembled from these full-disk extreme ultraviolet (EUV) image acquired throughout 2007, during which STEREO-A was positioned ahead of Earth in its heliocentric orbit.

2.3. *Coronal Magnetic Field Models*

2.3.1. *PFSS CMF Model*

The PFSS model extrapolates the solar coronal magnetic field by assuming a current-free approximation in the region between the photosphere and the source surface (Y. M. Wang & N. R. Sheeley 1992; H. Li et al. 2021). This assumption leads to the condition:

$$\nabla \times \boldsymbol{B} = 0, \tag{1}$$

consequently, the magnetic field $\boldsymbol{B}$ can be represented as the negative gradient of a scalar magnetic potential:

$$\boldsymbol{B} = -\nabla \Psi_B. \tag{2}$$

Combining with the divergence-free condition of magnetic field:

$$\nabla \cdot \boldsymbol{B} = 0, \tag{3}$$

yields Laplace's equation for the potential:

$$\nabla^2 \Psi_B = 0. \tag{4}$$

The general solution to Laplace's equation in spherical coordinates (r, θ, ϕ) takes the form of a spherical harmonic expansion (J. D. Jackson 1962):

$$\Psi_B(r,\theta,\phi) = \sum_{l=0}^{\infty} \sum_{m=-l}^{l} \left[f_l^m r^l + g_l^m r^{-(l+1)} \right] P_l^m(\cos\theta) e^{imf}, \tag{5}$$

where P_l^m are the Legendre polynomials, and the coefficients f_l^m, g_l^m are determined by boundary conditions. The model employs two physically motivated boundary conditions:

1. Photospheric Boundary ($r = R_\odot$):

The radial field component $B_r(R_\odot, \theta, \phi)$ is specified using synoptic magnetogram data, providing the primary input for the solution.

2. Source Surface Boundary ($r = R_{\mathrm{SS}}$):

On the source surface (conventionally $R_{\mathrm{SS}} = 2.5R_\odot$), the magnetic field is constrained to become purely radial:

$$B_\theta(R_{\mathrm{SS}}, \theta, \phi) = B_\phi(R_{\mathrm{SS}}, \theta, \phi) = 0. \tag{6}$$

2.3.2. *PFCS CMF model*

The PFCS model represents a refinement of the PFSS model by accounting for the horizontal current effect in the corona, and thus reproduce the latitudinally independent radial magnetic fields measured by Ulysses (E. J. Smith & A. Balogh 1995). Within the inner region ($r < R_{\mathrm{SS}}$), the PFCS model assumes that the CMFs are current free, which means that magnetic fields derive from a scalar potential. When transiting to the outer region ($R_{\mathrm{SS}} < r < R_{\mathrm{SCS}}$, with $R_{\mathrm{SCS}} = 13R_\odot$ being the outer boundary of the PFCS model), the potential extrapolation is also used, with the radial magnetic field B_r on the source surface serving as the lower boundary condition. To induce the horizontal current, a polarity reversal method is used in the outer region. Specifically, If $B_r > 0$ on the source surface, B_θ and B_ϕ are unchanged. If $B_r < 0$ on the source surface, $B_r = -B_r$, $B_\theta = -B_\theta$ and $B_\phi = -B_\phi$. The thin horizontal current sheet condition is introduced in the opposite field region (K. H. Schatten 1971):

$$\Psi_B(r,\theta,\phi) = R \sum_{l=0}^{\infty} \sum_{m=0}^{l} (\frac{R}{r})^{n+1} \left[g_l^m \cos(m\phi) + h_l^m sin(m\phi) \right] P_l^m(\theta), \tag{7}$$

where the coefficients g_l^m and h_l^m are determined by boundary conditions. The original orientations of the magnetic fields are restored after the magnetic fields are obtained in the outer region.

2.3.3. *CSSS CMF Model*

Unlike the PFSS and PFCS models, the CSSS model includes two spherical surfaces: the cusp surface (located at $r = R_{\mathrm{CS}}$, approximately the height of the cusp point of the coronal helmet streamers) and the source surface. From the solar surface to the cusp surface which is called the inner region, the scalar magnetic potential Ψ is expressed as (X. Zhao & J. T. Hoeksema 1994; X. Zhao & J. T. Hoeksema 1995; G. Shi et al. 2024):

$$\Psi_B(r,\theta,\phi) = \sum_{l=1}^{N_\odot} \sum_{m=0}^{l} R_l^\odot(r) P_l^m(\cos\theta) \left[g_{\mathrm{ml}}^\odot \cos(m\phi) + h_{\mathrm{ml}}^\odot sin(m\phi) \right], \tag{8}$$

$$R_l^\odot(r) = \frac{R_\odot(1+a)^n}{(n+1)(r+a)^{n+1}}, \tag{9}$$

where $N_\odot$ is the maximum principal index, the coefficients $g_{ml}^\odot$ and $h_{ml}^\odot$ are determined by the photospheric synoptic maps.

From the cusp surface to the source surface which is called the middle region, the magnetic fields gradually orient toward the radial direction. The scalar magnetic potential in this region satisfies (X. Zhao & J. T. Hoeksema 1994; X. Zhao & J. T. Hoeksema 1995; G. Shi et al. 2024):

$$\Psi_B(r,\theta,\phi) = \sum_{l=0}^{N_c}\sum_{m=0}^{l} R_l^c(r) P_l^m(\cos\theta)\left[g_{\mathrm{ml}}^c \cos(m\phi) + h_{\mathrm{ml}}^c sin(m\phi)\right], \tag{10}$$

$$R_{\mathrm{ml}}^c(r) = R_\odot \left[\frac{n+1}{R_{\mathrm{CS}}^2 (R_{\mathrm{CS}}+a)^n} + \frac{n(R_{\mathrm{CS}}+a)^{n+1}}{R_{\mathrm{CS}}^2 (R_{\mathrm{SS}}+a)^{2n+1}}\right]^{-1} \times \left[\frac{1}{(r+a)^{n+1}} - \frac{(r+a)^n}{(R_{\mathrm{SS}}+a)^{2n+1}}\right], \tag{11}$$

where N_c is the maximum principal index, the coefficients g_{ml}^c and h_{ml}^c are determined by boundary conditions on the cusp surface.

Beyond the source surface which is called the outer region, the magnetic fields are completely open and follow Parker spiral lines. According to G. Shi et al. (2024), we set the cusp surface height $R_{\mathrm{CS}} = 2.5R_\odot$, the source surface height $R_{\mathrm{SS}} = 13R_\odot$ and the current parameter $a = 1.0R_\odot$ in the CSSS model.

2.3.4. *Fisk CMF Model*

Fisk model assumes magnetic fields expand from polar coronal holes to the source surface symmetrically about the magnetic axis. L. A. Fisk (1996) proposed the transformation between the photosphere's footpoints and the source surface's footpoints. First, the footpoints on the source surface have heliomagnetic coordinate given by

$$\begin{aligned}
\theta_{\mathrm{ss}}^{\mathrm{hm}} &= \cos^{-1}(\sin(\theta_{\mathrm{ss}}^{\mathrm{hg}})\cos(\phi_{\mathrm{ss}}^{\mathrm{hg}})\sin(\alpha) + \cos(\theta_{\mathrm{ss}}^{\mathrm{hg}})\cos(\alpha)),\\
\phi_{\mathrm{ss}}^{\mathrm{hm}} &= \cos^{-1}(\frac{\sin(\theta_{\mathrm{ss}}^{\mathrm{hg}})\cos(\phi_{\mathrm{ss}}^{\mathrm{hg}})\cos(\alpha) - \cos(\theta_{\mathrm{ss}}^{\mathrm{hg}})\sin(\alpha)}{\sin(\theta_{\mathrm{ss}}^{\mathrm{hm}})}).
\end{aligned} \tag{12}$$

Then, based on the Divergence Theorem, the footpoints on the photosphere tracing from the source surface are obtained by

$$\begin{aligned}
\theta_{\mathrm{ph}}^{\mathrm{hm}} &= \sin^{-1}\left(\sqrt{\frac{(1-\cos(\theta_{\mathrm{ss}}^{\mathrm{hm}}))\sin^2(\theta_{\mathrm{ph}}^{\mathrm{mm}})}{(1-\cos(\theta_{\mathrm{ss}}^{\mathrm{mm}}))}}\right),\\
\phi_{\mathrm{ph}}^{\mathrm{hm}} &= \phi_{\mathrm{ss}}^{\mathrm{hm}}.
\end{aligned} \tag{13}$$

Finally, we can obtain the footpoints in the heliographic coordinate system by

$$\begin{aligned}
\theta_{\mathrm{ph}}^{\mathrm{hg}} &= \cos^{-1}(\cos(\theta_{\mathrm{ph}}^{\mathrm{hm}})\cos(\alpha) - \sin(\theta_{\mathrm{ph}}^{\mathrm{hm}})\cos(\phi_{\mathrm{ph}}^{\mathrm{hm}})\sin(\alpha)),\\
\phi_{\mathrm{ph}}^{\mathrm{hg}} &= \cos^{-1}(\frac{\sin(\theta_{\mathrm{ph}}^{\mathrm{hm}})\cos(\phi_{\mathrm{ph}}^{\mathrm{hm}})\cos(\alpha) + \cos(\theta_{\mathrm{ph}}^{\mathrm{hm}})\sin(\alpha)}{\sin(\theta_{\mathrm{ph}}^{\mathrm{hm}})}),
\end{aligned} \tag{14}$$

where the subscripts ss, ph, hg and hm represents the source surface, photosphere, heliographic coordinates, and heliomagnetic coordinates, respectively. $\theta_{\mathrm{ph}}^{\mathrm{mm}}$ and $\theta_{\mathrm{ss}}^{\mathrm{mm}}$ are chosen to be 24° and 70° (P. J. Steyn et al. 2024). It is worth noting that the Fisk coronal model only provides the correspondence between the source surface and the footpoints of the photosphere, and does not provide a specific expression for the coronal magnetic field.

2.4. *Heliospheric Magnetic Field Models*

2.4.1. *Parker HMF Model*

Parker HMF model describes the spiral structure imposed on the solar wind by the Sun's rotation E. N. Parker (1958). The field components in the Heliocentric Carrington Coordinate System are expressed as:

$$\begin{aligned}
B_r &= B_0(\frac{r_0}{r})^2\\
B_\theta &= 0\\
B_\phi &= -\frac{B_r r}{V}\Omega\sin\theta,
\end{aligned} \tag{15}$$

where B_0 represents the radial field strength at the reference distance r_0, V is the solar wind speed, Ω is the angular rotation velocity of the Sun; r, θ and ϕ are the heliospheric distance, colatitude, and longitude, respectively. The radial component B_r decays with the inverse square of heliocentric distance, reflecting magnetic flux conservation in a radially expanding solar wind of constant speed V. The azimuthal component B_ϕ emerges from the Ω, which causes the magnetic field lines to take an Archimedean spiral configuration.

2.4.2. *Fisk HMF Model*

Fisk model extends the classical Parker spiral by accounting for the sun's differential rotation on the photosphere and non-radial excursions. The HMF field components in the Heliocentric Carrington Coordinate System are detailed by T. H. Zurbuchen et al. (1997) as follows:

$$\begin{aligned} B_r &= B_0(\frac{r_0}{r})^2 \\ B_\theta &= \frac{B_0{r_0}^2}{Vr}\omega\sin\beta\sin(\phi+\frac{\Omega r}{V}-\phi_0) \\ B_\phi &= \frac{B_0{r_0}^2}{Vr}[\omega(\cos\beta\sin\theta+\sin\beta\cos\theta\cos(\phi+\frac{\Omega r}{V}-\phi_0))-\Omega\sin\theta], \end{aligned} \tag{16}$$

where B_0 represents the radial field strength at the reference distance r_0, V is the solar wind speed, Ω is the angular rotation velocity of the sun. The key parameters governing the magnetic field topology are: β is the polar angle between a magnetic field line p which originates from the rotational pole, after crossing the source surface and the axis of the rotation, ω is the differential rotation rate of the footpoints on the photosphere, α is the tilt angle of the solar magnetic axis relative to the rotation axis, ϕ_0 is the plane formed by the rotation axis and the magnetic axis. As previous works (R. J. Forsyth et al. 2002), we adapt the specific parameter values $\beta = 30°$, $\alpha = 15°$, $\omega = \frac{\Omega}{4}$ and $\phi_0 = 100°$.

3. RESULTS

We select three Carrington Rotations (CRs) to present detailed backmapping analysis: CR 2060 (August 14 - September 10, 2007), CR 2061 (September 10 - October 8, 2007), and CR 2064 (December 1 - December 29, 2007). During these periods, Ulysses was positioned at ~ 1.41, ~ 1.46, ~ 1.88 AU and latitudes of $3.3°N$ to $23.1°N$, $23.1°N$ to $42.1°N$, $70.1°N$ to $78.3°N$ respectively. Our solar wind backmapping methodology proceeds as follows: First, we quantify agreement in strength, polarity, and configuration between Parker/Fisk-predicted and Ulysses/Wind-observed HMFs. Then, we trace interplanetary solar wind back to CMF model boundaries using HMF models, evaluating spatial separations between Parker- and Fisk-mapped points. Finally, using the CMF models (PFSS, PFCS, CSSS, Fisk), we identify solar wind source locations, which are validated through EUVI observations. We also compare results across the CMF models.

3.1. *Mid-latitude and Ecliptic Backmapping*

To evaluate the fidelity of Parker and Fisk heliospheric HMF models, we compare predicted and observed HMF polarity, strength, and configuration in Figure 1. Panels (A) and (E) quantify polarity agreement (orange) and disagreement (green) between model predictions and spacecraft observations, determined through sign comparisons of the radial magnetic field component. For Ulysses' mid-latitude measurements, both models achieve identical polarity match rates of 83.61% with observations. In the ecliptic plane, Wind observations show 70.67% agreement with Parker predictions and 73.01% with Fisk predictions.

We show in Figure 1(B) and (F) one-hour-cadence (black dots) and filtered (light green dots) magnetic field strength measured by the Ulysses (B) and Wind (F) spacecraft as well as the magnetic field strength obtained from the Parker (pink dots) and Fisk models (lightskyblue dots). Raw magnetic field maps were preprocessed using Gaussian filtering to attenuate high-frequency noise while preserving field gradients. This operation was implemented via *scipy.ndimage.gaussian_filter* in Python, generating smoothed field strength distributions for subsequent analysis. The unsigned residual metric χ (G. Shi et al. 2024) is used to quantify the consistency of the magnetic field strength between measurements and models, and is defined by the expression:

$$\chi = \frac{1}{N}\sum_{i=1}^{N}\sqrt{(|M_i|-|O_i|)^2}, \tag{17}$$

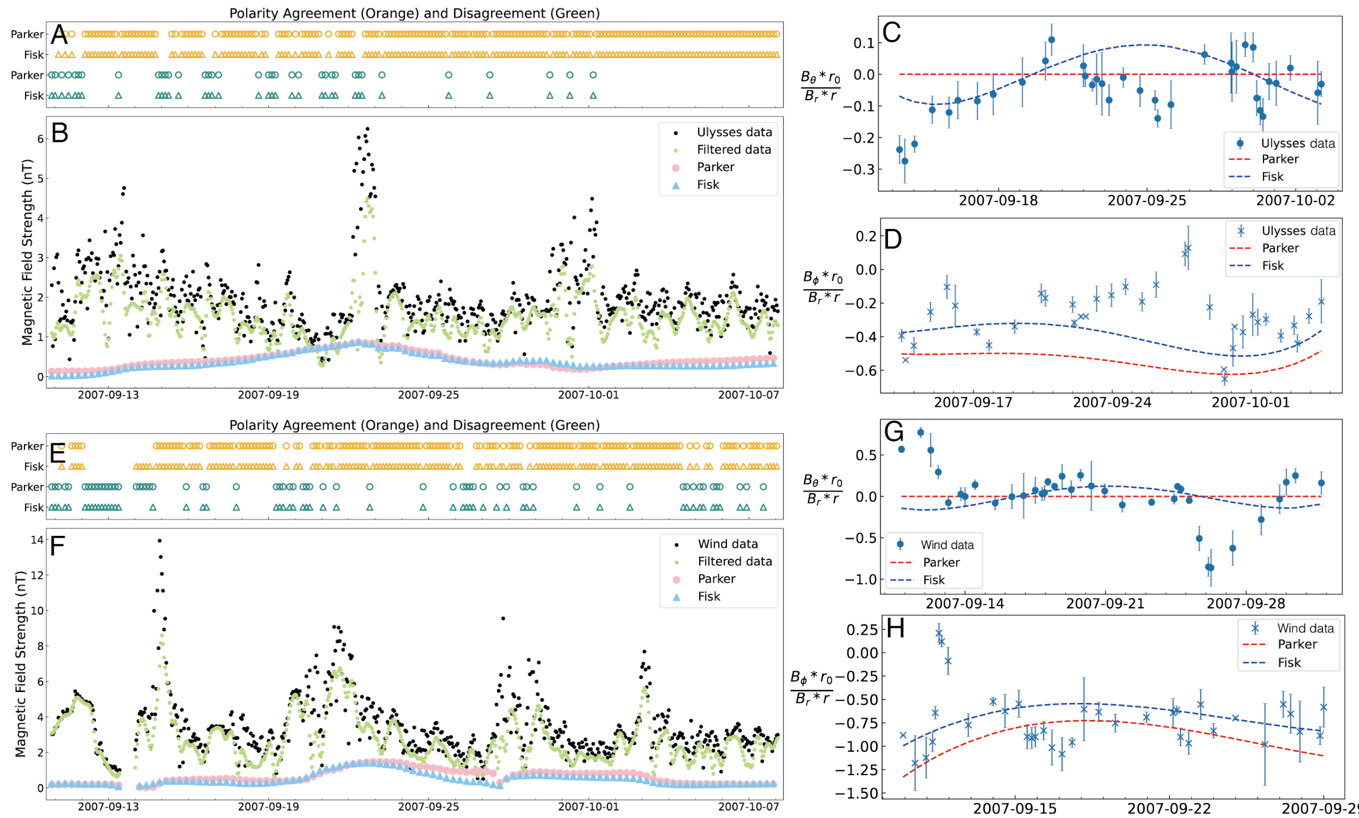

Figure 1. Predicted HMFs by the Parker and Fisk models with in situ measurements obtained from the Ulysses (A, B, C, D) and Wind (E, F, G, H). Panels A and E: the agreement (orange) and disagreement (green) between measured and predicted HMF polarity. Panels B and F: black dots and light green dots denote one-hour-cadence and filtered measured magnetic field strength, respectively; pink dots and lightskyblue dots shows the predicted magnetic field strength by the Parker and Fisk models, respectively. Panels C and G: the observed (circular markers) and predicted values (red dotted line for Parker and blue dotted line for Fisk) of $B_\theta * r_0/B_r * r$ (where $r_0 = 1$ AU and r is the heliocentric distance), representing the meridional magnetic field component B_θ divided by the radial magnetic field component B_r. Panels D and H: the same as Panels C and G but for azimuthal field component (B_ϕ).

where N is the number of measured data, M denotes the magnetic field strength of the predicted model, and O represents the filtered observational data. Smaller residual values indicate better agreement with observations.

For the mid-latitude measurements by Ulysses, the residuals for the Parker and Fisk models are 1.09 nT and 1.12 nT, respectively. In the ecliptic plane, the residuals for the Parker and Fisk models are 2.09 nT and 2.19 nT, respectively. The Parker and Fisk models exhibits better consistency with observations at the mid-latitude than at the ecliptic plane, though its predictions systematically underestimate the measured values.

Figure 1(C) and (G) display the observed (circular markers) and predicted values (red dotted line for Parker and blue dotted line for Fisk) of $B_\theta * r_0/B_r * r$ (where $r_0 = 1$ AU and r is the heliocentric distance), representing the meridional magnetic field component B_θ divided by the radial magnetic field component B_r. Figure 1(D) and (H) show the same as Figure 1(C) and (G) but for the azimuthal magnetic field component B_ϕ. $B_\theta * r_0/B_r * r$ and $B_\phi * r_0/B_r * r$ are calculated using the method described by T. H. Zurbuchen et al. (1997), following these steps:

1. High-frequency variations are suppressed using a Gaussian filter.
2. The Carrington longitudes on the source surface are computed from the in situ solar wind speed.
3. Data are binned into 10° Carrington longitude intervals.
4. A 3-point running average is applied for smoothing.

Error bars represent the standard error of the mean within each Carrington longitude bin.

While neither model fully captures the observed complexity of ecliptic plane to mid-latitude field configurations (J.-S. Park et al. 2025), the Fisk model demonstrates superior alignment with measurements in both amplitude and phase compared to the Parker model. This improvement is particularly evident in its representation of the meridional field component.

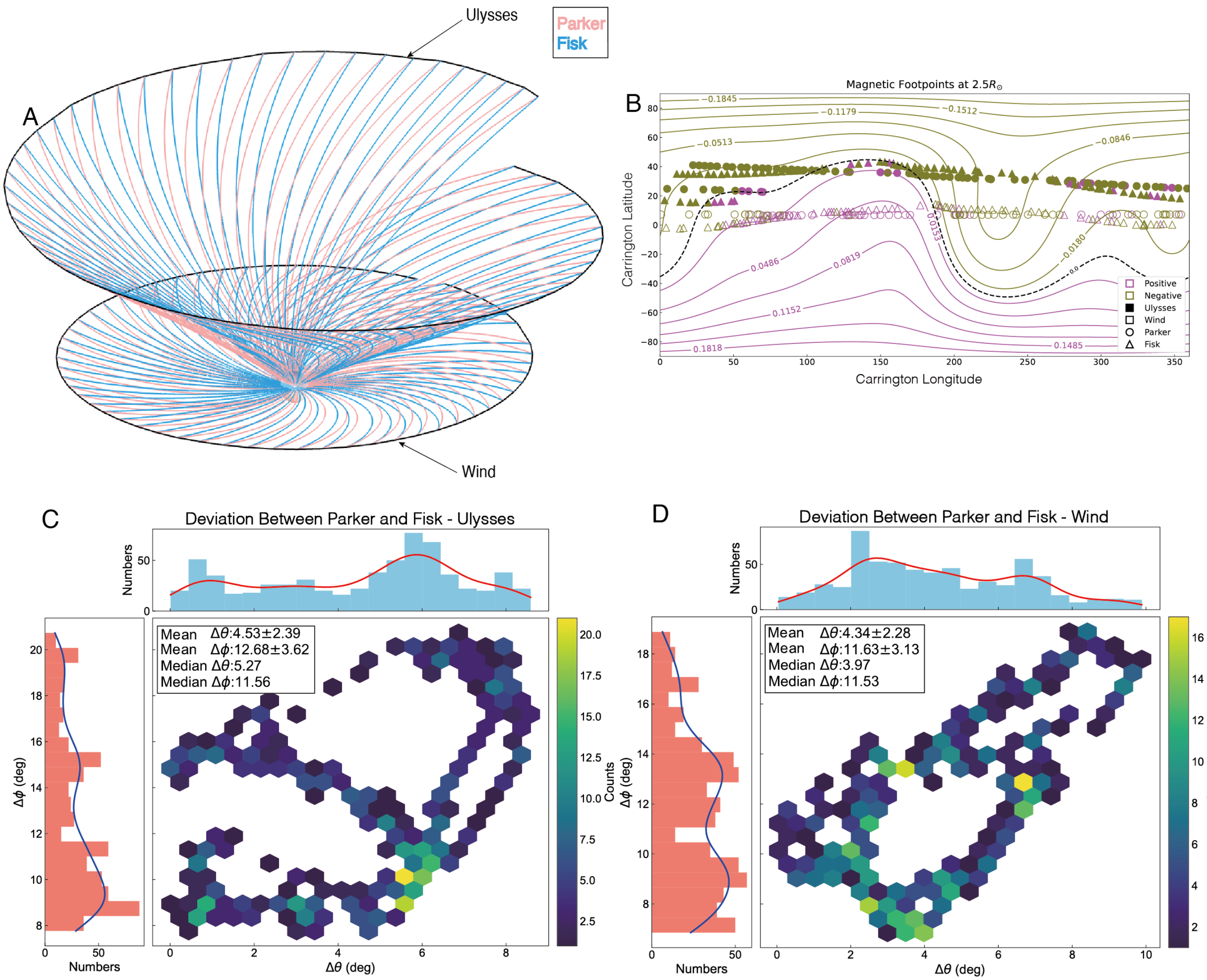

Figure 2. Backmapping of the solar wind measured by the Ulysses and Wind spacecraft to the source surface of the PFSS model ($2.5R_{\odot}$) based on the Parker and Fisk HMF model. Panel A: examples of Parker (red) and Fisk (blue) magnetic field lines traced from identical measurement points to $r = 2.5R_{\odot}$. Panel B: magnetic footpoints at $2.5R_{\odot}$ traced from measurements by Ulysses (solid markers) and Wind (hollow markers) using the Parker (circles) and Fisk (triangles) models. Color coding indicates polarity: olive for negative, magenta for positive, and black dotted lines for neutral line. Panel C: latitudinal ($\Delta\theta$) and longitudinal ($\Delta\phi$) deviations between Parker and Fisk magnetic footpoints at $r = 2.5R_{\odot}$, traced from Ulysses measurements. The color encodes the count. The blue and red lines overlaid on the histograms represent the smoothed probability density distributions of the deviation values, derived from Kernel Density Estimation (KDE). Panel D: the same as Panel C but for Wind measurements.

Figure 2 presents the backmapping of the solar wind measured by the Ulysses and Wind spacecraft to the source surface of the PFSS model, based on the Parker and Fisk HMF models. Figure 2(A) shows examples of Parker (red) and Fisk (blue) magnetic field lines traced from identical measurement points to $r = 2.5R_{\odot}$. Although both the Parker and Fisk fields form spirals around the Sun, the Fisk field diverges a little from the Parker field.

In Figure 2(B), we exhibit magnetic footpoints at $2.5R_{\odot}$ traced from measurements by Ulysses (solid markers) and Wind (hollow markers) using the Parker (circles) and Fisk (triangles) models. Polarity is color-coded: olive for negative, magenta for positive, with the neutral line indicated by a black dotted line. Figure 2(B) reveals that the

Ulysses measurements map back to regions of negative polarity. In contrast, the Wind measurements are divided by the large-scale heliospheric current sheet (HCS), placing one part in positive polarity regions and the other in negative polarity regions. Furthermore, magnetic field footpoints at $2.5R_{\odot}$ connected to Ulysses and Wind by the Parker fields exhibit slight deviations from those mapped using the Fisk fields.

We quantify the deviations of magnetic field footpoints at $2.5R_{\odot}$ between the Parker and Fisk fields in Figure 2(C) and (D), which show that for Ulysses (mid-latitude) and Wind (ecliptic plane) measurements, the latitudinal differences between magnetic footpoint positions obtained by Parker and Fisk fields range from $\Delta\theta = 0°$ to $\Delta\theta =\sim 10°$. The mean values are $4.53° \pm 2.39°$ (Ulysses) and $4.34° \pm 2.28°$ (Wind), with median values being 5.27° and 3.97°, respectively. The longitudinal differences exhibit a broader spread from $\Delta\phi = 0°$ to $\Delta\phi =\sim 20°$, with averages of $12.68° \pm 3.62°$ (Ulysses) and $11.63° \pm 3.13°$ (Wind), and median values of 11.56° (Ulysses) and 11.53° (Wind).

Following a comparative analysis of the Parker and Fisk HMF models, we utilize the boundary footpoints derived from the Fisk HMF model within the CMF model for subsequent backmapping to the solar surface. The results are presented in Figure 3. Figure 3(A) illustrates representative magnetic field lines from the PFSS (pink), PFCS (darkviolet), and CSSS (mediumseagreen) models. Figure 3(B) and (C) show the corresponding photospheric footpoints traced from the Ulysses and Wind in situ observations, overlaid on a synoptic magnetogram, respectively.

The magnetic field line connectivity predicted by the CMF models exhibits significant variation. For Ulysses mid-latitude measurements, most solar wind maps to high latitudes. While the footpoints obtained using the PFSS, PFCS, and CSSS models converge spatially, those predicted by the Fisk model deviate evidently from the PFSS, PFCS, and CSSS models.

For Wind ecliptic measurements, the mapping results are more complex, with all four models predicting markedly different connectivity. In some cases, the PFSS and Fisk models map the solar wind to sources in the northern hemisphere, whereas the PFCS and CSSS models map the same wind to the southern hemisphere. Furthermore, instances occur where the PFSS, PFCS, and CSSS models map to the same active region, yet connect to footpoints of opposing magnetic polarities.

Figure 3(D) displays a view of the Sun's north pole created by reprojecting the STEREO-A/SECCHI EUVI 195 Å synoptic map onto a spherical coordinate system, alongside backmapped solar wind source regions color-coded by speed during Ulysses' mid-latitude scan. Coronal holes, which are characterized by relatively low EUV emissions due to reduced plasma density, constitute the primary source of the Sun's open magnetic field (J. B. Zirker 1977). All four CMF models predict that the fast solar wind measured by Ulysses originates from polar coronal holes. This aligns with established research indicating that the fast solar wind (> 700 km s^{-1}) originates from polar coronal holes (J. Phillips et al. 1995; M. Neugebauer et al. 1998; R. Lionello et al. 2005; M. A. Reiss et al. 2021).

Figure 3(E) presents backmapped source regions of the Wind-measured solar wind superimposed on EUV full-disk images. To further contextualize these source regions, Figure 4 shows corresponding footpoints overlaid on an EUVI synoptic map. The PFSS, PFCS, and CSSS models map portions of the solar wind to both mid/low-latitude coronal holes and the periphery of the north polar coronal hole. Notably, the PFSS model associates fast solar wind (> 500 km s^{-1}) with low-latitude coronal holes or active regions, whereas PFCS and CSSS models connect some fast wind streams to the polar coronal hole boundary. In contrast, the Fisk model uniquely predicts some of low-latitude solar wind sources within quiet-Sun regions exhibiting high EUV emissions.

Figures 5 and 6 present latitudinal ($\Delta\theta$) and longitudinal ($\Delta\phi$) deviations of photospheric footpoints among the PFSS, PFCS, and CSSS models for Ulysses and Wind measurements, respectively. Representative magnetic field lines traced from identical points at the model outer boundaries to the photosphere are included for contextual comparison.

For Ulysses mid-latitude measurements, angular deviations between models are minimal. The closest agreement occurs between the PFCS and CSSS models, with mean deviations of $1.66° \pm 0.63°$ in latitude and $1.03° \pm 0.73°$ in longitude, and median deviations of 1.76° and 0.82°, respectively. Larger but moderate differences are observed between other pairs: mean $\Delta\theta = 6.09° \pm 2.38°$ (median: 6.13°), mean $\Delta\phi = 5.37° \pm 2.63°$ (median: 6.19°) between the PFSS and PFCS models, and mean $\Delta\theta = 4.41° \pm 2.36°$ (median: 4.39°), mean $\Delta\phi = 4.90° \pm 2.43°$ (median: 5.40°) between the PFSS and CSSS models.

In contrast, Wind ecliptic measurements exhibit substantial model divergence, with maximum deviations reaching up to 40° ($\Delta\phi$) and 80° ($\Delta\theta$). Latitudinal differences systematically exceed longitudinal variations across all model comparisons. Notably, PFCS-CSSS pairs maintain minimal separation, consistent with mid-latitude backmapping trends.

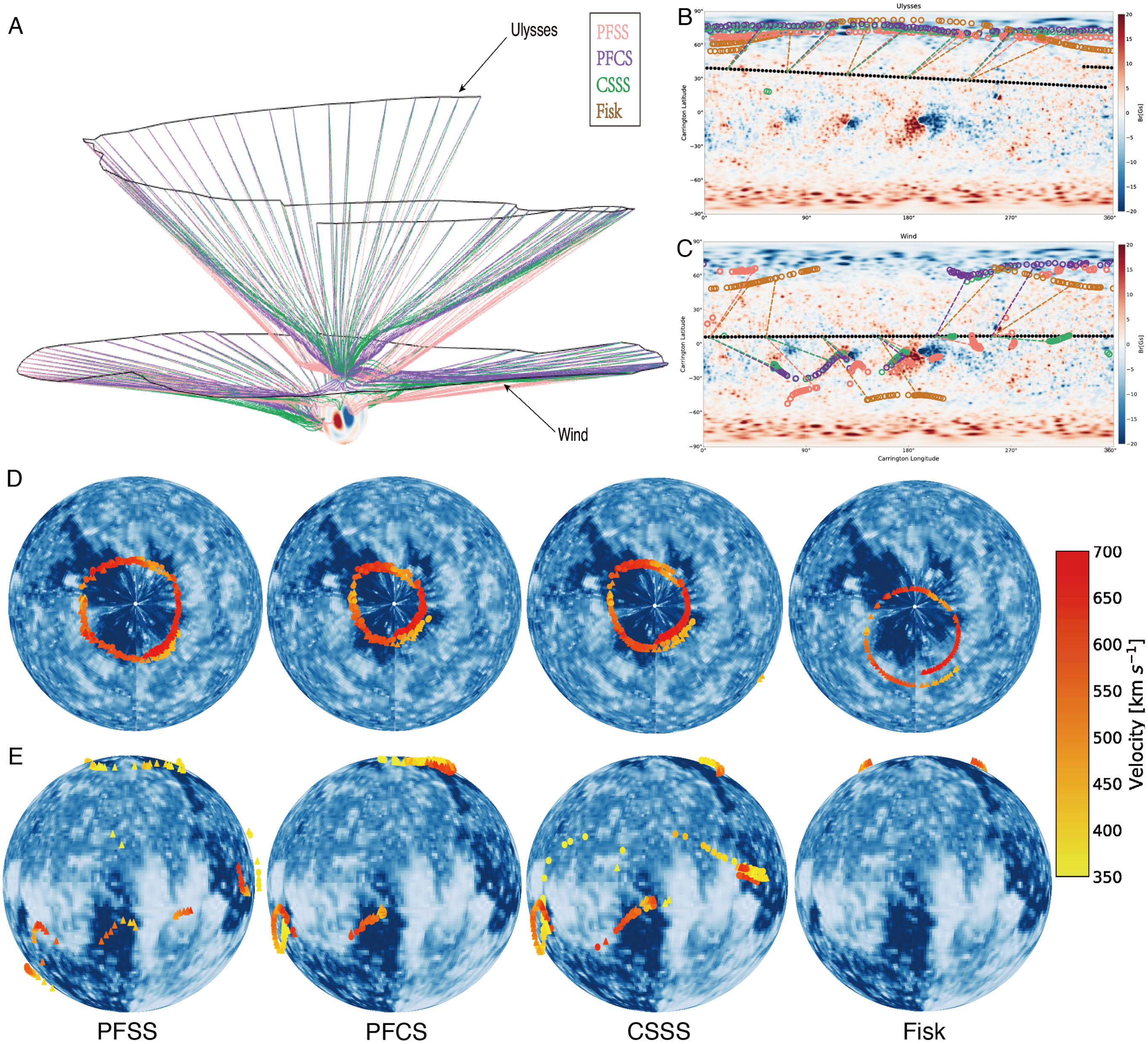

Figure 3. Backmapping of the solar wind measured by the Ulysses and Wind spacecraft from the source surface ($2.5R_{\odot}$) to the photosphere based on the Fisk HMF model. Panel A: representative magnetic field lines from the PFSS (pink), PFCS (darkviolet), and CSSS (mediumseagreen) CMF models. Panels B and C: corresponding photospheric footpoints traced from the Ulysses (B) and Wind (C) in situ observations, overlaid on a synoptic magnetogram, respectively. Panel D: A view of the Sun's north pole created by reprojecting the STEREO-A/SECCHI EUVI 195 Å synoptic map onto a spherical coordinate system, with backmapped solar wind source regions color-coded by speed during Ulysses' mid-latitude scan. Panel E: the same as Panel D but for Wind measurements.

3.2. *High- and Low-latitude Backmapping*

We extend our validation to CR 2060 (low-latitude focused, 14 August - 10 September 2007) and CR 2064 (high-latitude focused, 1-29 December 2007), maintaining identical methodology as previously defined in the ecliptic and middle latitudes.

Figure 7 evaluates the Parker and Fisk HMF model predictions of HMFs' polarity, strength, and configuration against Ulysses measurements at both high and low latitudes. Figure 7(A) and (B) demonstrate strong agreement at high latitudes, with both models achieving 92.52% polarity match rates with observations. Residual field strengths

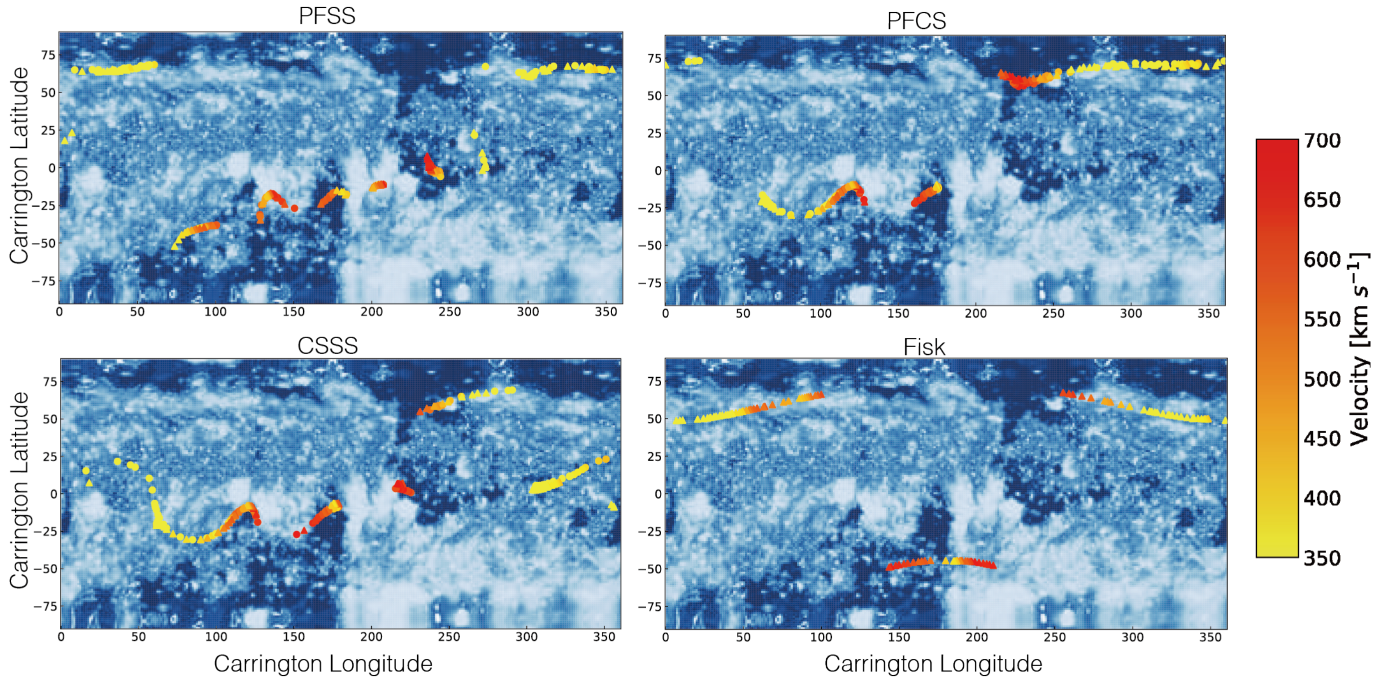

Figure 4. Backmapped source regions of the Wind-measured solar wind superimposed on an EUVI synoptic image.

remain minimal (Parker: 0.18 nT; Fisk: 0.19 nT), indicating excellent consistency between predicted and observed magnitudes. As quantified by the configuration metrics $B_\theta r_0/(B_r r)$ and $B_\phi r_0/(B_r r)$ in Figure 7(C) and (D), the Fisk model successfully captures the global trend of high-latitude measured magnetic topology despite localized deviations.

Figure 7 panels (E-H) evaluate Parker and Fisk HMF model performance against Ulysses low-latitude measurements, with comparative metrics benchmarked to Wind ecliptic measurements (corresponding to Figure 1(E-H)). The Parker model achieves 65.60% polarity agreement with Ulysses observations, while the Fisk model shows a significant improvement, reaching 72.48%. The residual field strengths is 1.84 nT for the Parker fields and 1.94 nT for the Fisk fields. While neither model fully captures the complexity of low-latitude field configurations, the Fisk model demonstrates comparatively better alignment with the Ulysses low-latitude measurements.

Figure 8 compares backmapped footpoint locations at the PFSS source surface ($2.5R_\odot$) for Ulysses high- and low-latitude measurements using the Parker versus Fisk HMF models. Although both models predict similar large-scale magnetic topologies, their derived footpoints exhibit significant spatial separations across for the Ulysses high- and low-latitude measurements. These separations show isotropic scattering across the $\Delta\theta$-$\Delta\phi$ plane. The mean longitudinal deviation between the Parker and Fisk HMF models is as high as $18.67° \pm 13.53°$ for the high-latitude measurements, and $18.58° \pm 3.39°$ for the low-latitude measurements, with median longitudinal deviation being 14.92° and 18.72°, respectively. While latitudinal offsets remain consistently smaller than longitudinal deviations for both regimes, they still reach mean (median) values of several degrees.

Figure 9 presents backmapped source regions of Ulysses high- and low-latitude solar wind using the PFSS, PFCS, CSSS, and Fisk CMF models. For high-latitude measurements, the PFSS, PFCS, and CSSS models show minimal field line divergence, with most photospheric footpoints clustered near the latitude of 85°. EUVI imagery in Figure 9 confirms these models map the fast solar wind(> 750 km s^{-1}) back to the central region of the northern polar coronal hole. The Fisk model places footpoints farther from the pole (consistent with its underlying assumptions), with some even extending to the boundary of the coronal hole.

For Ulysses low-latitude measurements, magnetic connectivity exhibits significant divergence among PFSS, PFCS, and CSSS models, resulting in substantial spatial separation of photospheric footpoints across all three solutions as shown in Figure 9(C). These conventional models map most low-speed solar wind (< 500 km s^{-1}) to the periphery of the northern polar coronal hole as shown in Figure 9(E). Notably, the PFSS, PFCS, and CSSS models associate some low-speed wind with isolated low-latitude coronal holes, while the Fisk model exclusively links all such wind to polar coronal holes.

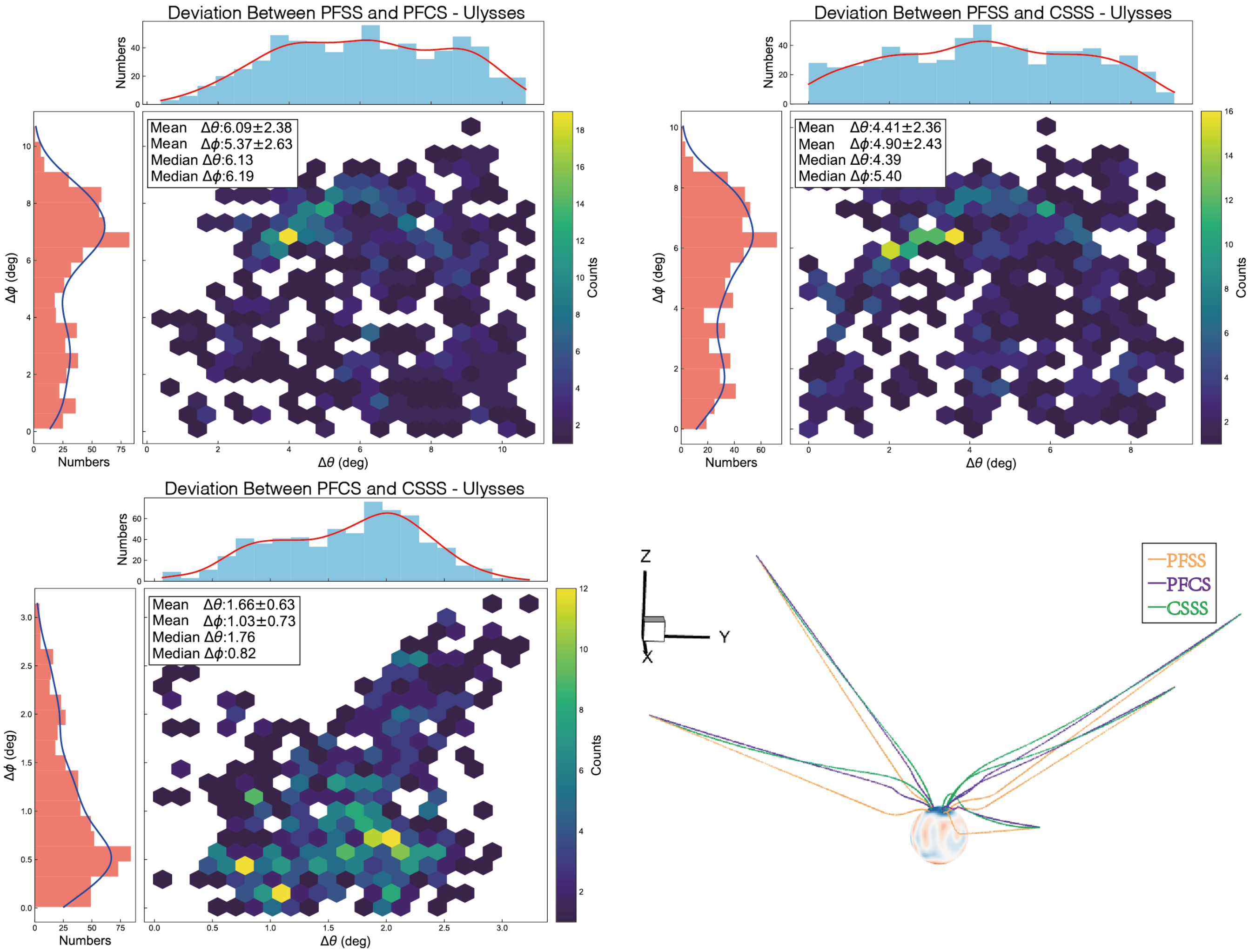

Figure 5. Latitudinal ($\Delta\theta$) and longitudinal ($\Delta\phi$) deviations of photospheric footpoints among the PFSS, PFCS, and CSSS models for Ulysses measurements. Representative magnetic field lines traced from identical points at the model outer boundaries to the photosphere are included for contextual comparison.

Figure 10 presents the latitudinal ($\Delta\theta$) and longitudinal ($\Delta\phi$) deviations of photospheric footpoints among the PFSS, PFCS, and CSSS models for Ulysses high- and low-latitude measurements. For Ulysses high-latitude measurements, the angular separations between the models are widely scattered across the $\Delta\theta$-$\Delta\phi$ plane. The mean and median $\Delta\theta$ values are significantly smaller than those of $\Delta\phi$. Similarly, the PFCS and CSSS models exhibit the closest agreement. For low-latitude measurements, the angular separations predominantly cluster within a narrow range of small $\Delta\theta$ and $\Delta\phi$ values. However, some cases exist where deviations between the models reach 50° in longitude ($\Delta\phi$) and 120° in latitude ($\Delta\theta$).

3.3. *Backmapping with Different Source Surface Heights*

In the PFSS CMF model, the source surface height $R_{\rm SS}$ represents a critical yet empirically constrained parameter that can significantly influences reconstructed coronal magnetic field topologies and subsequent solar wind predictions (A. Koukras et al. 2025). Adjusting $R_{\rm SS}$ can directly modulates the extent of closed fields and the distribution of open fields. This sensitivity necessitates careful optimization of $R_{\rm SS}$ to reconcile model outputs with in situ solar wind measurements and remote-sensing observations (e.g., white-light coronagraphs or EUV coronal hole boundaries). Here, we investigate how variations in $R_{\rm SS}$ affect the identification of solar wind source regions.

Figure 11 compares observed and predicted HMF polarity and strength using mid-latitude and ecliptic measurements from Ulysses and Wind. The models employed are the PFSS CMF model coupled with Parker's HMF model, tested

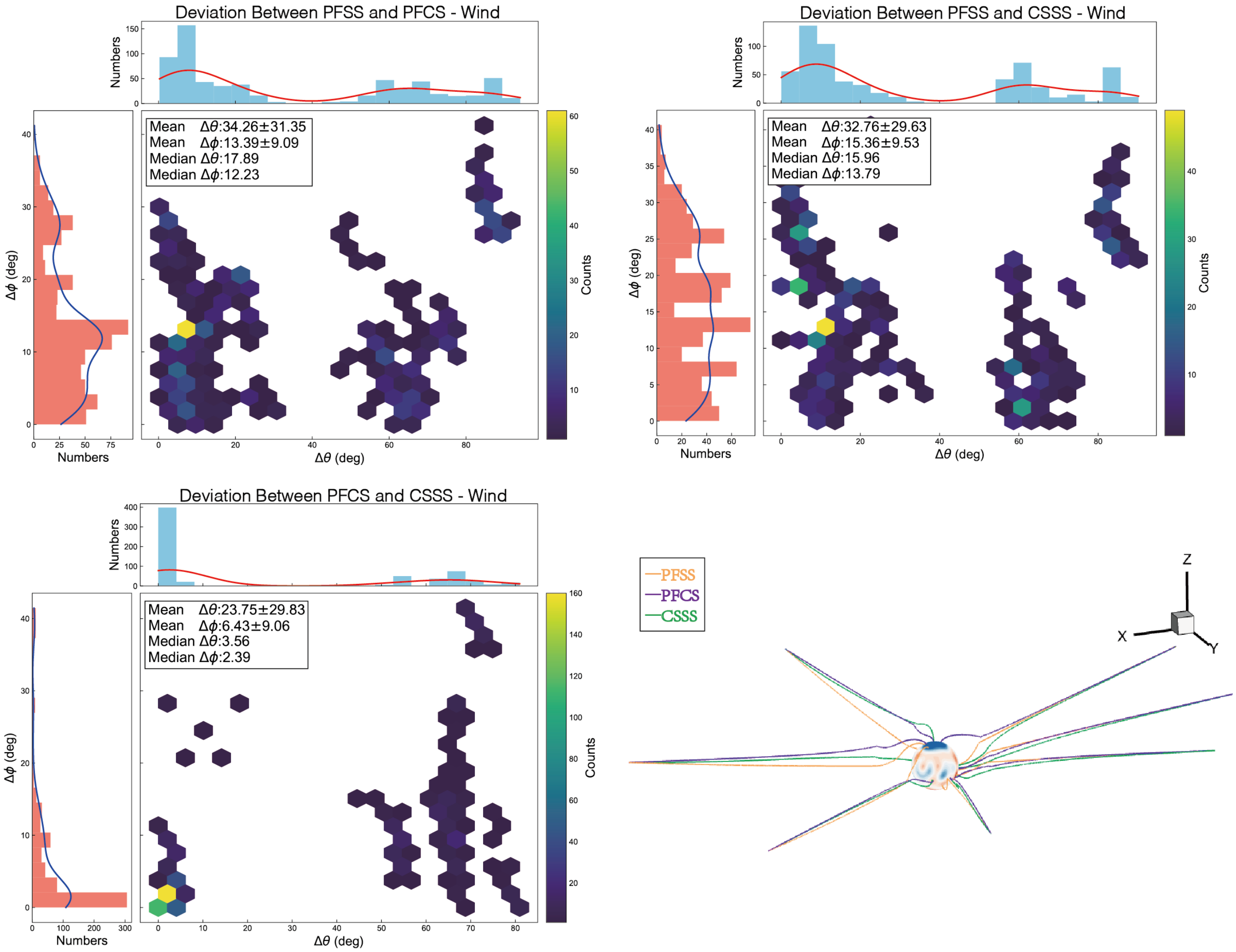

Figure 6. The same as Figure 5 but for Wind measurements.

at source surface heights of $R_{\rm SS} = 2.0R_\odot$, $R_{\rm SS} = 2.5R_\odot$, $R_{\rm SS} = 3.0R_\odot$ and $R_{\rm SS} = 3.5R_\odot$. Variations in $R_{\rm SS}$ have limited impact on mid-latitude HMF predictions: all four cases achieve similar polarity match rates and residual field strengths relative to observations. For ecliptic HMFs, polarity match rates remain comparable across $R_{\rm SS}$ values, while residual field magnitudes increase from 1.97 nT for $R_{\rm SS} = 2.0R_\odot$ to 2.26 nT for $R_{\rm SS} = 3.5R_\odot$. Consistent with this trend, lower $R_{\rm SS}$ values yield stronger ecliptic HMFs.

Figure 12 shows photospheric footpoints locations derived from Ulysses mid-latitude and Wind ecliptic measurements according to the different heights of the source surface. The left column overlays the footpoints on GONG synoptic magnetograms, while the right column uses EUVI synoptic maps. Variations in the source surface height induce more pronounced changes in footpoint locations for ecliptic measurements than for mid-latitude observations. For the ecliptic solar wind, the PFSS model with $R_{\rm SS} = 2.0R_\odot$ maps some sources to mid-latitudes, while these same sources shift to high latitudes by the other three cases. The identical ecliptic solar wind is mapped back to the quiet-Sun region with $R_{\rm SS} = 2.0R_\odot$, and back to the active region with $R_{\rm SS} = 2.5R_\odot$, and to a mid-latitude coronal hole with $R_{\rm SS} = 3.0R_\odot$ and $R_{\rm SS} = 3.5R_\odot$. Mid-latitude solar wind sources consistently map near polar coronal hole boundaries across all $R_{\rm SS}$ values. However, at $R_{\rm SS} = 2.0R_\odot$, a subset shifts to low-latitude quiet-Sun regions.

Figure 13 presents latitudinal ($\Delta\theta$) and longitudinal ($\Delta\phi$) deviations of photospheric footpoints among the different source surface heights for Ulysses mid-latitude (up panels) and Wind ecliptic (down panels) measurements. For Ulysses mid-latitude measurements, footpoints converge toward consistent locations at $R_{\rm SS} \geq 2.5R_\odot$. The mean (median) deviation between successive heights is $1.60° \pm 0.43°$ $(1.56°)$ in latitude and $1.56° \pm 1.23°$ $(1.29°)$ in longitude between

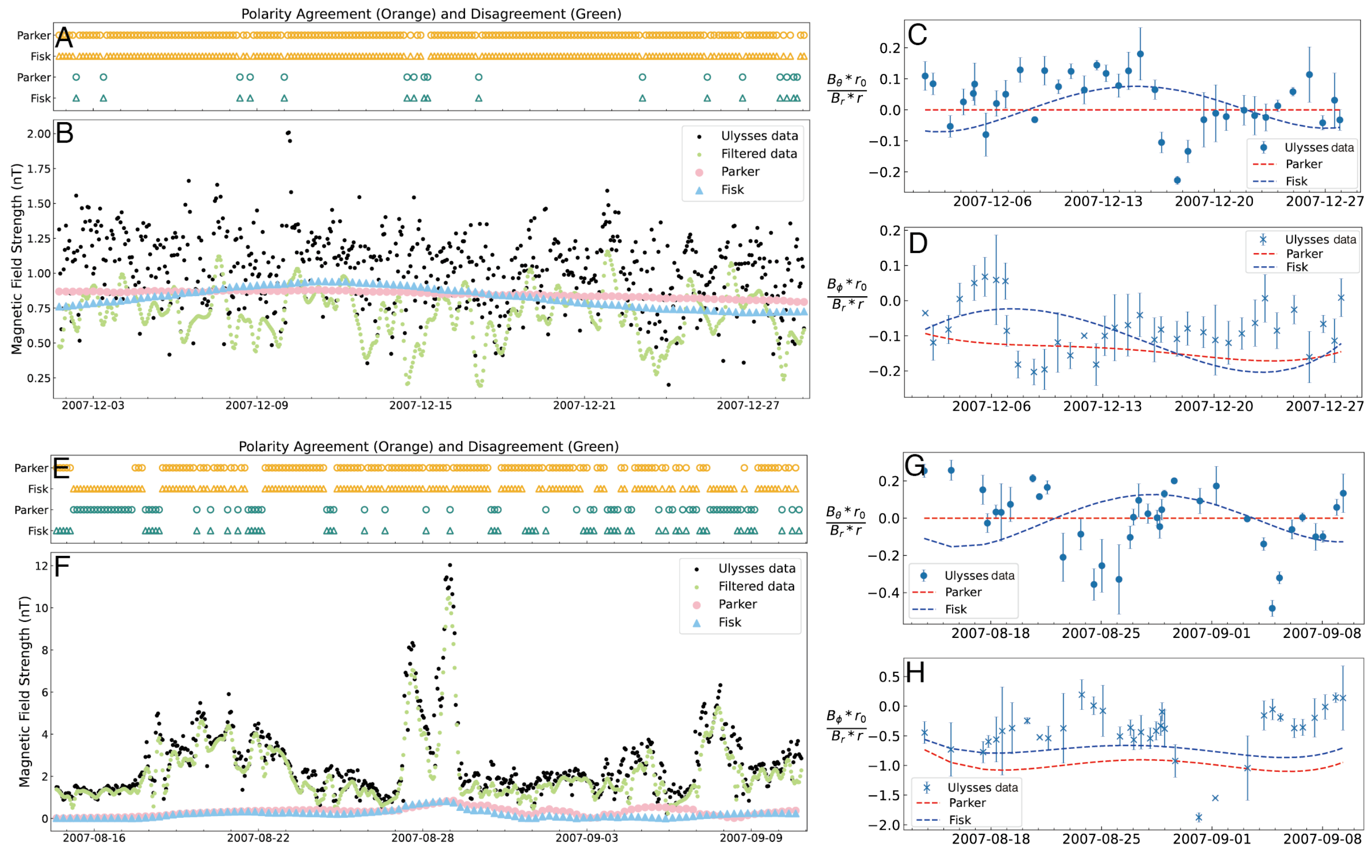

Figure 7. The same as Figure 1 but for high- (A, B, C, D) and low-latitude (E, F, G, H) measurements by Ulysses.

$R_{SS} = 2.5R_\odot$ and $R_{SS} = 3.0R_\odot$, and is $2.78° \pm 0.65°$ ($2.74°$) in latitude and $2.77° \pm 1.97°$ ($2.26°$) in longitude between $R_{SS} = 2.5R_\odot$ and $R_{SS} = 3.5R_\odot$. Although large differences exist between $R_{SS} = 2.0R_\odot$ and $R_{SS} = 2.5R_\odot$, angular separations remain confined within narrow $\Delta\theta$-$\Delta\phi$ ranges. For Wind ecliptic measurements, deviations between R_{SS} pairs (e.g., $2.0R_\odot$ vs. $2.5R_\odot$) exhibit bimodal distribution: predominantly small angular differences with occasional large separations ($> 50°$).

4. CONCLUSIONS AND DISCUSSION

In this study, we combined the Parker and Fisk HMF models with the PFSS, PFCS, and CSSS CMF models to trace the solar wind back to the solar disk. Our analysis, leveraging in situ Ulysses measurements across latitudes, GONG ADAPT synoptic magnetograms, STEREO-A EUVI observations, demonstrates that the specific configurations of both the CMF and HMF models significantly influence the identification of solar wind source regions. Crucially, we quantified angular deviations in the backmapping results arising from different CMF/HMF combinations, with particular implications for accurately pinpointing the origins of fast solar wind emanating from the Sun's polar regions.

Our analysis reveals performance differences between the Parker and Fisk HMF models across latitudes (see Table 1). Both models achieve similar polarity match rates and residual field strengths relative to Ulysses measurements, with the higher consistency between predicted and measured HMFs at high latitudes than at low latitudes. Although the Fisk HMF model improves upon the Parker model in representing the meridional field component, it is unable to fully capture the complex structure of the HMF across the full latitudinal range. Critically, when tracing solar wind measurements back to the coronal source surface ($2.5R_\odot$), the Fisk HMF model produces significantly displaced magnetic footpoints compared to the Parker model, despite similar overall HMF configurations. Latitudinal offsets between the two models' footpoints average several degrees, with a comparable median value, confirming that these offsets are substantially smaller than the longitudinal deviations. Furthermore, the longitudinal deviation between the Parker and Fisk models exhibits a clear positive trend with increasing latitude, a feature that is robustly captured by both the rising mean values and the closely aligned median values.

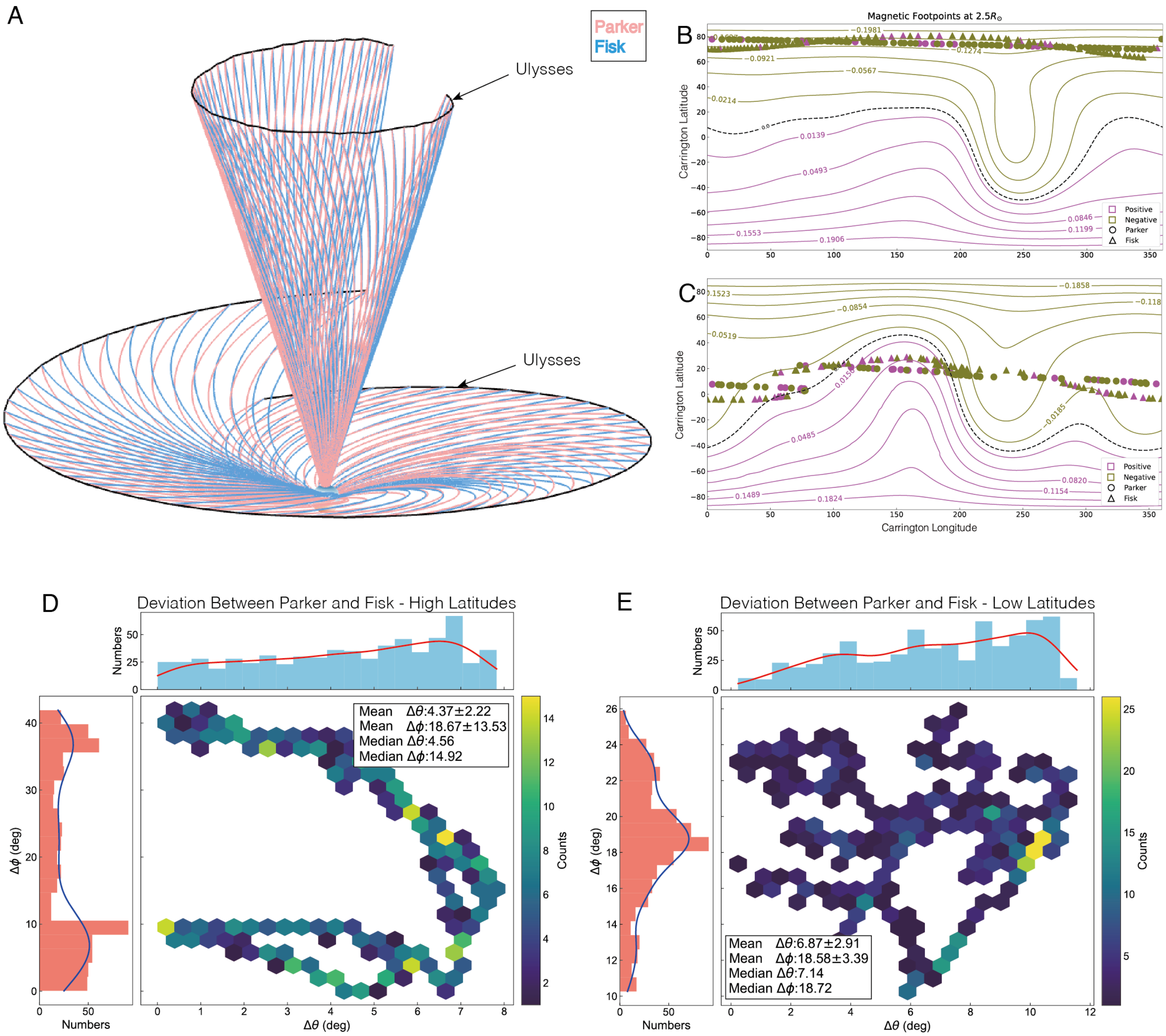

Figure 8. The same as Figure 2 but for high- and low-latitude measurements by Ulysses.

With the HMF model held constant, the PFSS, PFCS, and CSSS CMF models yield significantly different solar wind source region derivations (see Tables 2 and 3). The latitudinal separations ($\Delta\theta$) show a distinct pattern. At high latitudes, both the mean and median $\Delta\theta$ across models are typically on the order of several degrees. At low latitudes, the averaged $\Delta\theta$ reaches several tens of degrees, while the median $\Delta\theta$ is several degrees in most cases. Longitudinal variations ($\Delta\phi$) demonstrate another pattern: at both high and low latitudes, the mean and median $\Delta\phi$ are about tens of degrees, while at mid-latitude, both statistical measures diminish to only several degrees. Furthermore, a comparison of model agreements shows that the PFCS and CSSS models exhibit the closest agreement in both mean and median deviations, whereas the PFSS and PFCS models show the greatest divergence across all metrics.

When coupling the PFSS CMF model with the Parker HMF model, we find that the source surface height $R_{\rm SS}$ modulates the identification of solar wind source regions. Variations in $R_{\rm SS}$ have minimal impact on predicting mid-latitude HMF polarity and strength, as evidenced by both the mean and median latitudinal and longitudinal deviations between successive heights remaining within a few degrees and showing close agreement. This indicates a convergence toward consistent mid-latitude solar wind sources for $R_{\rm SS} \geq 2.5R_\odot$. In contrast, ecliptic solar wind sources exhibit

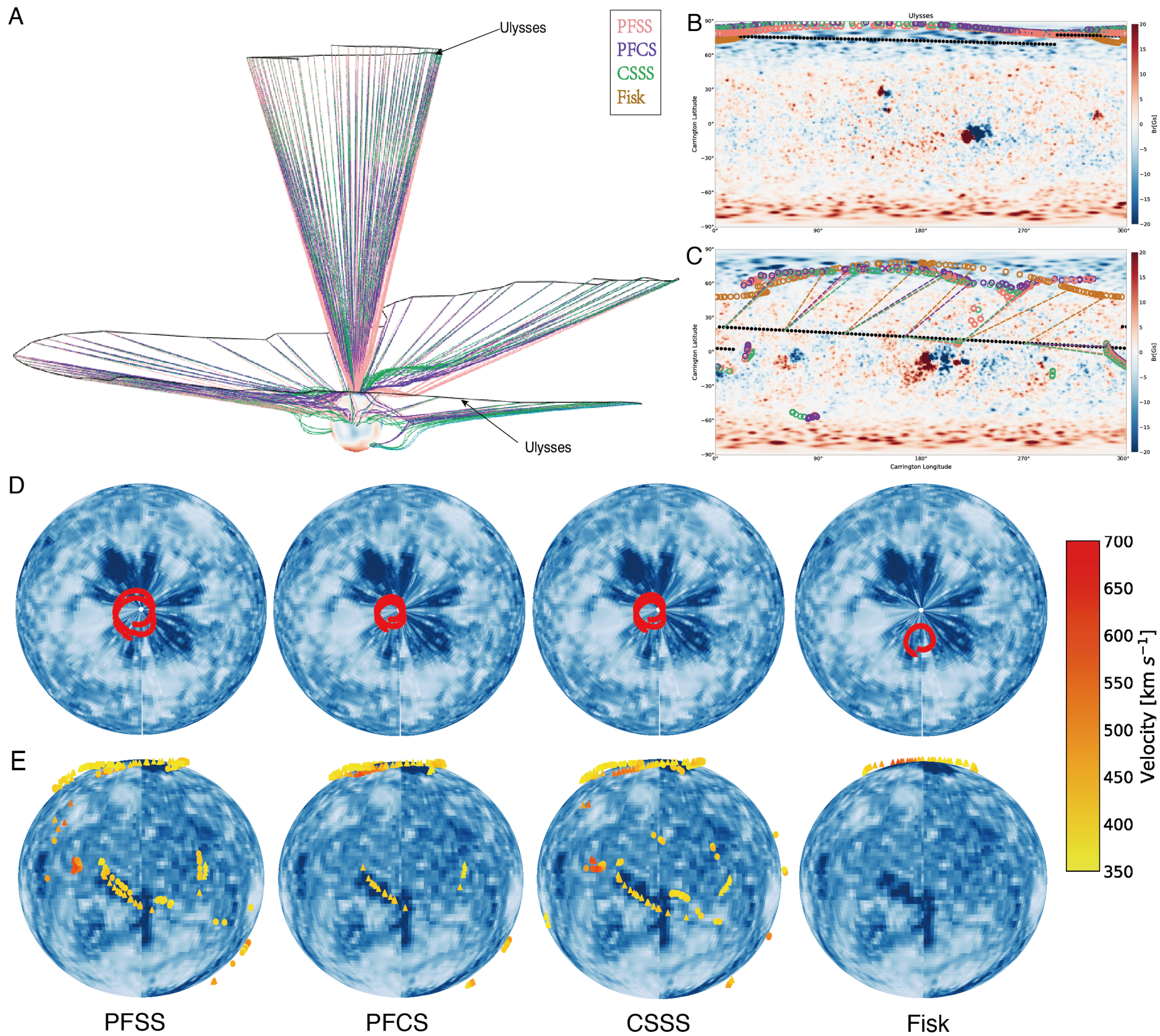

Figure 9. The same as Figure 3 but for high- and low-latitude measurements by Ulysses.

a pronounced dependence on R_{SS}. At $R_{SS} = 2.0R_{\odot}$, for instance, the solar wind maps to mid-latitudes or quiet-Sun regions, whereas higher R_{SS} values map it to high latitudes or active regions. The median latitudinal deviation in the ecliptic, while smaller than the mean, remains substantially larger than the mid-latitude values. Notably, angular deviations between different R_{SS} pairs follow the bimodal distribution: most frequently small separations coexist with less frequent but substantial divergences ($> 50°$).

This study provides a comprehensive quantification of how the interplay between coronal and heliospheric magnetic field models influences the uncertainty and reliability of solar wind source region identification. The inherent model-dependent variability should be acknowledged and quantified when interpreting backmapping results for specific solar wind streams or correlating in situ measurements with solar source features. For polar coronal hole wind studies, simple models like PFSS coupled with Parker may be reasonably adequate, supported by the relative robustness of high-latitude source identification across the CMF models and the higher consistency of the HMF predictions with measurements. Conversely, low-latitude/ecliptic solar wind exhibits the heightened sensitivity to model choices, underscoring the challenges in pinpointing the origins of the slow solar wind stemming from its complex and likely

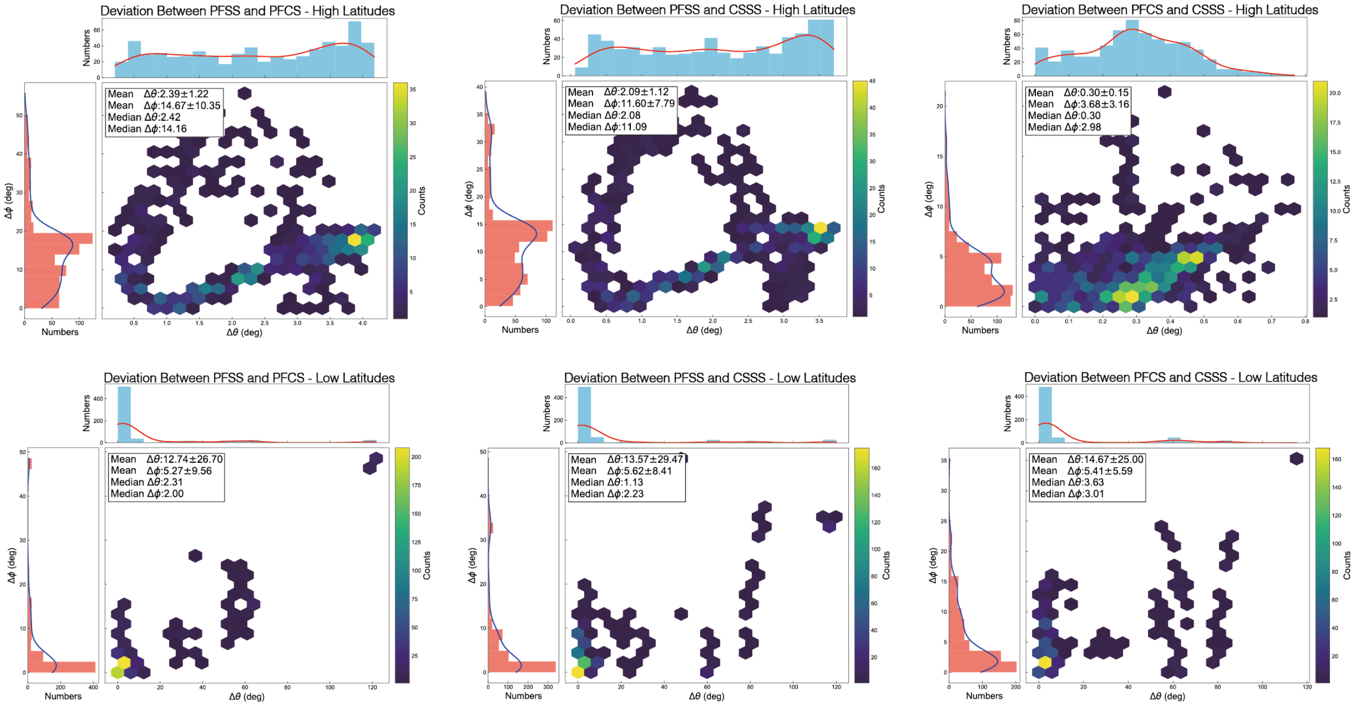

Figure 10. Latitudinal ($\Delta\theta$) and longitudinal ($\Delta\phi$) deviations of photospheric footpoints among the PFSS, PFCS, and CSSS models for Ulysses high-(up panels) and low-latitude (down panels) measurements.

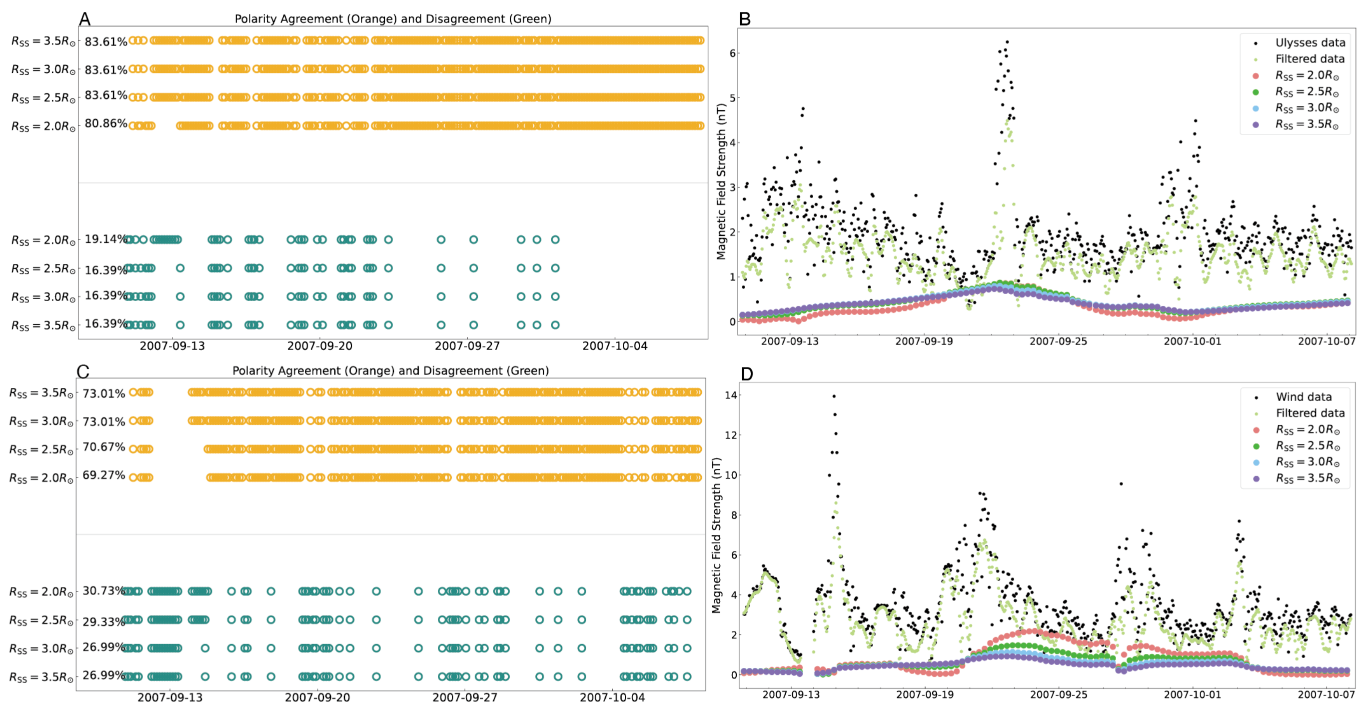

Figure 11. Observed and predicted HMF polarity and strength with in situ measurements obtained from Ulysses and Wind.

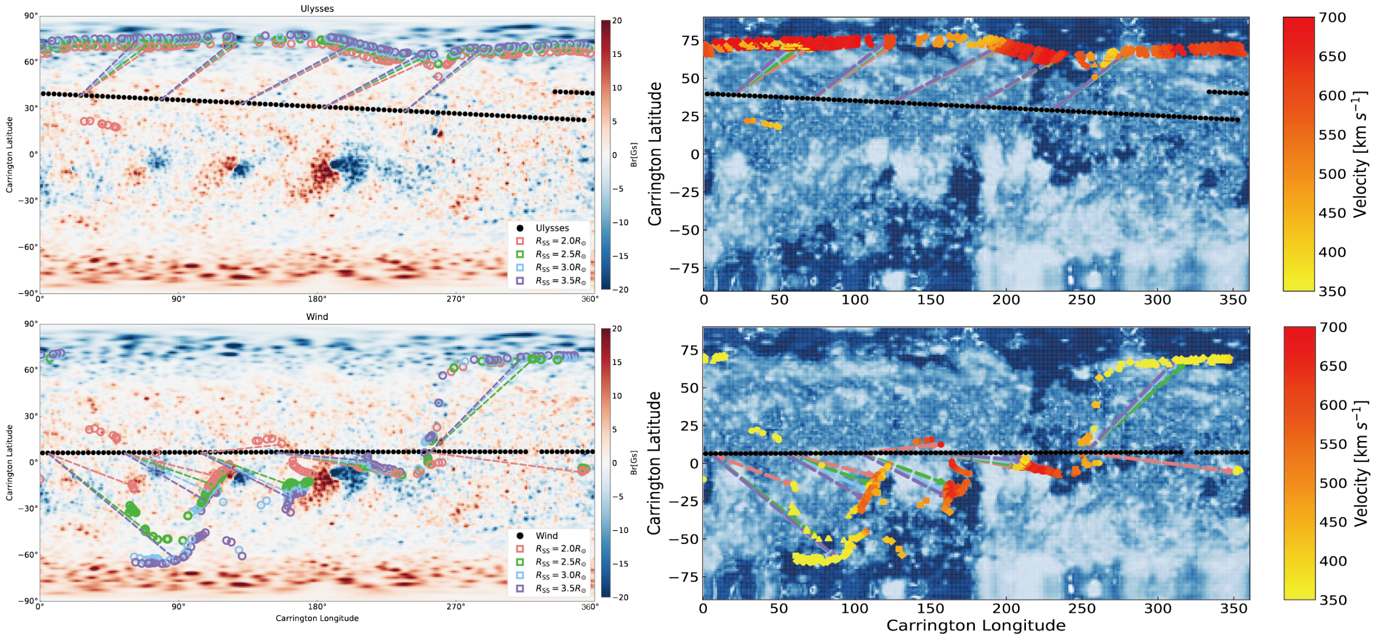

Figure 12. Photospheric footpoints traced from the different source surface of the PFSS model on the GONG synoptic magnetogram and EUVI synoptic map.

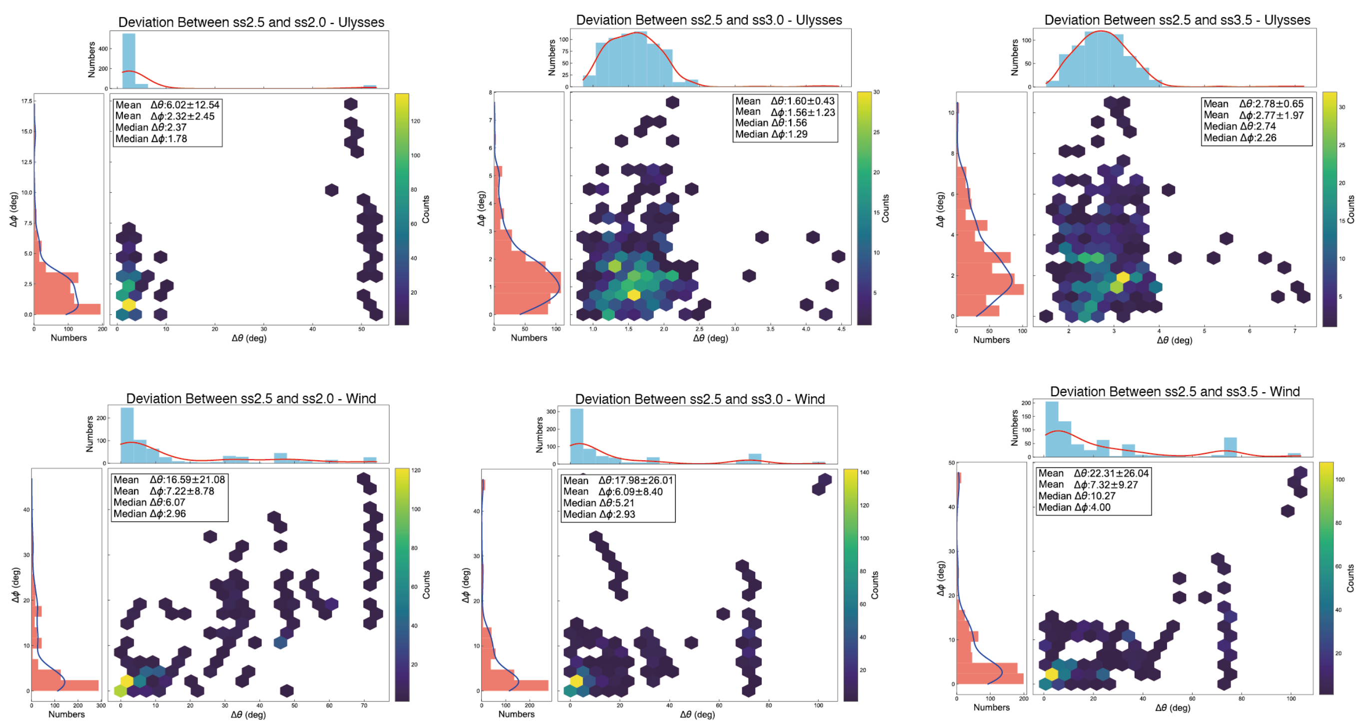

Figure 13. Latitudinal ($\Delta\theta$) and longitudinal ($\Delta\phi$) deviations of photospheric footpoints among the different source surface of the PFSS model for Ulysses mid-latitude (up panels) and Wind ecliptic (down panels) measurements.

multi-source nature (P. Riley & R. Lionello 2011; H. Fu et al. 2015; L. Abbo et al. 2016; S. R. Cranmer et al. 2017; N. M. Viall & J. E. Borovsky 2020; H. Tian et al. 2021). Our future works include to investigate the formation and evolution of co-rotation interaction region and their impact on solar wind backmapping using the adaptive mesh refinement solar-interplanetary space-time conservation element and solution element (AMR-SIP-CESE) solar wind numerical model (X. Feng et al. 2010, 2012; L. P. Yang et al. 2012; L. Yang et al. 2023, 2025).

Table 1. Difference Between the Parker and Fisk HMF Models in Prediction and Footpoint Positions.

Latitude	Heliospheric magnetic field models	Consistency of magnetic field strength	The polarity agreement between footpoints and in-situ measures	Latitudinal and longitudinal separation of footpoints on the source surface	
				Mean values	Median values
74N-79N (CR2066)	Fisk	0.15	90.63%	5.22±2.58	5.83
	Parker	0.13	90.63%	27.35±15.60	25.99
69N-78N (CR2064)	Fisk	0.18	92.52%	4.37±2.22	4.56
	Parker	0.19	92.52%	18.67±13.53	14.92
77S-79S (CR2053)	Fisk	0.17	82.87%	5.87±3.48	6.05
	Parker	0.17	82.87%	35.22±18.84	35.31
41N-56N (CR2062)	Fisk	0.49	97.24%	3.98±1.88	4.41
	Parker	0.45	97.24%	11.16±5.12	10.37
22N-41N (CR2061)	Fisk	1.12	83.61%	4.53±2.39	5.27
	Parker	1.09	83.61%	12.68±3.62	11.56
35S-50S (CR2057)	Fisk	0.70	86.12%	4.06±1.97	4.62
	Parker	0.68	86.12%	10.63±4.35	10.43
2N-22N (CR2060)	Fisk	1.94	72.48%	6.87±2.91	7.14
	Parker	1.84	65.60%	18.58±3.39	18.72
6N-7N (CR2061-WIND)	Fisk	2.19	73.01%	4.34±2.28	3.97
	Parker	2.09	70.67%	11.63±3.13	11.53
17.5S-2N (CR2059)	Fisk	1.42	69.77%	5.82±3.07	6.49
	Parker	1.30	80.00%	15.51±3.69	14.83

In conclusion, while models provide essential tools for connecting the Sun and the heliosphere, our results demonstrate that significant uncertainties in solar wind source identification arise directly from the choice of coronal and heliospheric magnetic field models and their parameters. Acknowledging, quantifying, and understanding these uncertainties, as initiated here, is crucial for the accurate interpretation of solar wind measurements and the advancement of reliable space weather prediction.

ACKNOWLEDGMENTS

This work is supported by the National Key R&D Program of China (Nos. 2022YFF0503800), China's Space Origins Exploration Program, the National Natural Science Foundation of China (Nos. 42274213, 42474216, 42030204) and the Climbing Program of NSSC (E4PD3001). The work was carried out at National Supercomputer Center in Tianjin, China, and the calculations were performed on TianHe-1 (A). We gratefully acknowledge the use of data from the following sources. We thank the Global Oscillation Network Group (GONG) for their open-data use policy. We thank the SPDF team for providing these data through the COHOWeb service. We acknowledge the Ulysses Data System (UDS) for providing the data utilized in this study. We thank the NASA Wind mission team for the Wind spacecraft data used in this study, obtained via the NASA CDAWeb service (https://cdaweb.gsfc.nasa.gov). Data were provided by the STEREO/SECCHI consortium, comprising NRL, LMSAL, NASA/GSFC (US), RAL, UBHAM (UK), MPS (Germany), CSL (Belgium), IOTA, and IAS (France).

REFERENCES

Abbo, L., Ofman, L., Antiochos, S. K., et al. 2016, SSRv, 201, 55, doi: 10.1007/s11214-016-0264-1

Altschuler, M., & Newkirk, G. 1969, Sol Phys, 9, 131, doi: 10.1007/BF00145734

Table 2. Separation and Position of Photospheric Footpoints among the PFSS, PFCS, and CSSS CMF Models under the Fisk HMF Model.

Latitude	Latitudinal and longitudinal separation of footpoints at the photosphere between			Footpoint position					
				active region or coronal hole			quiet-Sun region		
	PFSS&PFCS (Mean values, Median values)	PFSS&CSSS (Mean values, Median values)	PFCS&CSSS (Mean values, Median values)	PFSS	PFCS	CSSS	PFSS	PFCS	CSSS
74N-79N (CR2066)	2.26±1.52, 2.27 13.57±8.92, 12.46	1.87±1.23, 1.88 10.98±7.17, 9.88	0.40±0.30, 0.32 2.97±1.94, 3.03	100%	100%	100%	0	0	0
69N-78N (CR2064)	2.39±1.22, 2.42 14.67±10.35, 14.16	2.09±1.12, 2.08 11.6±7.79, 11.09	0.30±0.15, 0.30 3.68±3.16, 2.98	100%	100%	100%	0	0	0
77S-79S (CR2053)	1.61±0.96, 1.68 13.05±16.21, 7.62	1.31±0.72, 1.52 9.18±14.81, 4.10	0.39±0.31, 0.36 4.80±3.71, 3.59	100%	100%	100%	0	0	0
41N-56N (CR2062)	4.09±0.85, 4.03 4.25±2.19, 4.64	2.92±0.81, 2.87 3.38±1.71, 3.65	1.18±0.39, 1.24 1.22±0.81, 1.19	100%	100%	100%	0	0	0
22N-41N (CR2061)	6.09±2.38, 6.13 5.37±2.63, 6.19	4.41±2.36, 4.39 4.90±2.43, 5.40	1.66±0.63, 1.76 1.03±0.73, 0.82	100%	100%	100%	0	0	0
35S-50S (CR2057)	5.55±6.17, 4.27 4.02±2.21, 4.18	4.20±6.10, 3.11 2.85±2.32, 2.56	1.35±0.57, 1.36 1.78±1.55, 1.22	87.54%	93.15%	90.34%	12.46%	6.85%	9.66%
2N-22N (CR2060)	12.74±26.7, 2.31 5.27±9.56, 2.00	13.57±29.47, 1.13 5.62±8.41, 2.23	14.67±25, 3.63 5.41±5.59, 3.01	95.57%	95.41%	92.05%	4.43%	4.59%	7.95%
6N-7N (CR2061-WIND)	34.26±31.35, 17.89 13.39±9.09, 12.23	32.76±29.63, 15.96 15.36±9.53, 13.79	23.75±29.83, 3.56 6.43±9.06, 2.39	95.01%	90.95%	89.55%	4.99%	9.05%	10.45%
17.5S-2N (CR2059)	7.76±16.21, 2.36 6.51±13.46, 0.92	5.42±9.40, 2.16 5.43±12.07, 0.98	8.63±15.78, 1.37 8.42±15.53, 0.87	98.14%	98.14%	96.74%	1.86%	1.86%	3.26%

Arge, C. N., Henney, C. J., Koller, J., et al. 2010, AIP Conference Proceedings, 1216, 343, doi: 10.1063/1.3395870

Arge, C. N., & Pizzo, V. J. 2000, Journal of Geophysical Research: Space Physics, 105, 10465, doi: https://doi.org/10.1029/1999JA000262

Bale, S. D., Drake, J. F., McManus, M. D., et al. 2023, Nature, 618, 252, doi: 10.1038/s41586-023-05955-3

Balogh, A., Beek, T. J., Forsyth, R. J., et al. 1992, A&AS, 92, 221

Balogh, A., & Erdõs, G. 2013, SSRv, 176, 177, doi: 10.1007/s11214-011-9835-3

Bizien, N., Froment, C., Madjarska, M. S., Dudok de Wit, T., & Velli, M. 2025, A&A, 694, A181, doi: 10.1051/0004-6361/202452140

Burger, R. A., Krüger, T. P. J., Hitge, M., & Engelbrecht, N. E. 2008, The Astrophysical Journal, 674, 511, doi: 10.1086/525039

Cranmer, S. R. 2025, Solar Wind Origin, https://arxiv.org/abs/2507.13460

Cranmer, S. R., Gibson, S. E., & Riley, P. 2017, SSRv, 212, 1345, doi: 10.1007/s11214-017-0416-y

Dakeyo, J.-B., Badman, S. T., Rouillard, A. P., et al. 2024, A&A, 686, A12, doi: 10.1051/0004-6361/202348892

Deng, Y., Tian, H., Jiang, J., et al. 2025, Chinese Journal of Space Science, 45, 1, doi: 10.11728/cjss2025.04.2025-0054

Ervin, T., Jaffarove, K., Badman, S. T., et al. 2024, ApJ, 975, 156, doi: 10.3847/1538-4357/ad7d00

Feng, X., Yang, L., Xiang, C., et al. 2012, SoPh, 279, 207, doi: 10.1007/s11207-012-9969-9

Feng, X., Yang, L., Xiang, C., et al. 2010, ApJ, 723, 300, doi: 10.1088/0004-637X/723/1/300

Fisk, L. A. 1996, Journal of Geophysical Research: Space Physics, 101, 15547, doi: https://doi.org/10.1029/96JA01005

Fisk, L. A., Zurbuchen, T. H., & Schwadron, N. A. 1999, The Astrophysical Journal, 521, 868, doi: 10.1086/307556

Table 3. Separation and Position of Photospheric Footpoints among the PFSS, PFCS, and CSSS CMF Models under the Parker HMF Model.

Latitude	Latitudinal and longitudinal separation of footpoints at the photosphere between			Footpoint position					
				active region or coronal hole			quiet-Sun region		
	PFSS&PFCS	PFSS&CSSS	PFCS&CSSS						
	(Mean values, Median values)	(Mean values, Median values)	(Mean values, Median values)	PFSS	PFCS	CSSS	PFSS	PFCS	CSSS
74N-79N (CR2066)	2.20±1.35, 1.77 20.52±16.84, 15.00	1.68±0.99, 1.30 12.89±8.43, 11.77	0.56±0.56, 0.41 9.92±10.70, 6.21	100%	100%	100%	0	0	0
69N-78N (CR2064)	2.12±0.64, 2.00 15.19±9.57, 14.13	1.80±0.58, 1.70 11.77±7.34, 10.79	0.32±0.19, 0.27 3.83±3.24, 2.90	100%	100%	100%	0	0	0
77S-79S (CR2053)	1.31±0.72, 1.25 33.06±41.50, 16.80	0.98±0.50, 0.89 16.29±18.30, 9.83	0.53±0.48, 0.37 21.62±38.24, 6.00	100%	100%	100%	0	0	0
41N-56N (CR2062)	7.98±2.67, 8.25 10.17±9.89, 5.81	4.72±1.50, 4.71 4.95±3.71, 4.46	3.62±2.39, 3.51 6.82±7.54, 3.80	100%	100%	100%	0	0	0
22N-41N (CR2061)	5.82±2.52, 5.99 5.26±2.76, 5.74	4.18±2.51, 4.44 4.94±2.64, 4.71	1.74±0.64, 1.77 1.08±0.70, 0.95	100%	100%	100%	0	0	0
35S-50S (CR2057)	8.85±2.99, 8.74 5.57±4.76, 4.35	4.80±1.68, 4.54 2.56±1.73, 2.24	4.23±2.58, 4.16 4.08±4.48, 2.53	88.47%	100%	100%	11.53%	0	0
2N-22N (CR2060)	25.89±29.88, 5.88 6.86±7.85, 5.32	20.06±26.05, 3.28 8.43±9.43, 4.97	20.80±25.75, 3.33 9.08±10.06, 4.69	85.93%	90.37%	86.24%	14.07%	9.63%	13.76%
6N-7N (CR2061-WIND)	32.91±33.42, 10.68 14.85±11.08, 12.33	33.89±30.33, 22.34 15.37±8.70, 14.51	22.82±26.54, 4.18 5.75±7.64, 2.69	90.80%	93.45%	80.97%	9.20%	6.55%	19.03%
17.5S-2N (CR2059)	7.50±13.97, 2.80 9.88±16.32, 2.94	4.81±7.43, 2.26 5.30±10.90, 1.43	8.32±14.06, 2.59 11.55±16.98, 3.27	99.54%	99.24%	94.11%	0.46%	0.76%	5.89%

Forsyth, R. J., Balogh, A., & Smith, E. J. 2002, Journal of Geophysical Research (Space Physics), 107, 1405, doi: 10.1029/2001JA005056

Fu, H., Li, B., Li, X., et al. 2015, Solar Physics, 290, 1399, doi: 10.1007/s11207-015-0689-9

Hou, C., He, J., Duan, D., et al. 2024a, Nature Astronomy, 8, 1246, doi: 10.1038/s41550-024-02321-9

Hou, C., Rouillard, A. P., He, J., et al. 2024b, ApJL, 968, L28, doi: 10.3847/2041-8213/ad4eda

Howard, R. A., Moses, J. D., Vourlidas, A., et al. 2008, Space Science Reviews, 136, 67, doi: 10.1007/s11214-008-9341-4

Jackson, J. D. 1962, Classical Electrodynamics (Wiley). https://ui.adsabs.harvard.edu/abs/1962clel.book.....J

King, J. H., & Papitashvili, N. E. 2020, OMNI Combined Heliopheric Observations (COHO), Merged Magnetic Field, Plasma and Ephermeris, Definitive Hourly Data, doi: 10.48322/6FFX-3441

Koskela, J., Virtanen, I., & Mursula, K. 2019, A&A, 631, A17, doi: 10.1051/0004-6361/201935967

Koukras, A., Dolla, L., & Keppens, R. 2025, Astronomy & Astrophysics, 694, A134, doi: 10.1051/0004-6361/202244327

Kumar, P., Karpen, J. T., Uritsky, V. M., et al. 2023, ApJL, 951, L15, doi: 10.3847/2041-8213/acd54e

Levine, R. H., Altschuler, M. D., & Harvey, J. W. 1977, J. Geophys. Res., 82, 1061, doi: 10.1029/JA082i007p01061

Li, H., Feng, X., & Wei, F. 2021, Journal of Geophysical Research (Space Physics), 126, e28870, doi: 10.1029/2020JA028870

Lin, R., Luo, Z., He, J., et al. 2024, Space Weather, 22, e2023SW003561, doi: https://doi.org/10.1029/2023SW003561

Linker, J. A., Mikić, Z., Biesecker, D. A., et al. 1999, J. Geophys. Res., 104, 9809, doi: 10.1029/1998JA900159

Lionello, R., Riley, P., Linker, J. A., & Mikić, Z. 2005, The Astrophysical Journal, 625, 463, doi: 10.1086/429268

Macneil, A. R., Owens, M. J., Finley, A. J., & Matt, S. P. 2021, Monthly Notices of the Royal Astronomical Society, 509, 2390, doi: 10.1093/mnras/stab2965

Müller, D., St. Cyr, O. C., Zouganelis, I., et al. 2020, A&A, 642, A1, doi: 10.1051/0004-6361/202038467

Neugebauer, M., Forsyth, R. J., Galvin, A. B., et al. 1998, J. Geophys. Res., 103, 14587, doi: 10.1029/98JA00798

Neugebauer, M., Forsyth, R. J., Galvin, A. B., et al. 1998, Journal of Geophysical Research: Space Physics, 103, 14587, doi: https://doi.org/10.1029/98JA00798

Nolte, J., & Roelof, E. 1973, Sol Phys, 33, 241, doi: 10.1007/BF00152395

Owens, M., & Forsyth, R. 2013, Sol. Phys., 10, doi: https://doi.org/10.12942/lrsp-2013-5

Parenti, S., Chifu, I., Del Zanna, G., et al. 2021, SSRv, 217, 78, doi: 10.1007/s11214-021-00856-1

Park, J.-S., Shi, Q., Seough, J., et al. 2025, The Astrophysical Journal Supplement Series, 280, 2, doi: 10.3847/1538-4365/adea79

Parker, E. N. 1958, ApJ, 128, 664, doi: 10.1086/146579

Peleikis, T., Kruse, M., Berger, L., & Wimmer–Schweingruber, R. F. 2017, Astronomy and Astrophysics, 602. https://api.semanticscholar.org/CorpusID:59431158

Phillips, J., Bame, S., Feldman, W., et al. 1995, Advances in Space Research, 16, 85, doi: https://doi.org/10.1016/0273-1177(95)00318-9

Pizzo, V. J. 1981, J. Geophys. Res., 86, 6685, doi: 10.1029/JA086iA08p06685

Posner, A., Zurbuchen, T. H., Schwadron, N. A., et al. 2001, J. Geophys. Res., 106, 15869, doi: 10.1029/2000JA000112

Reiss, M. A., Muglach, K., Möstl, C., et al. 2021, The Astrophysical Journal, 913, 28, doi: 10.3847/1538-4357/abf2c8

Riley, P., & Lionello, R. 2011, Solar Physics, 270, 575, doi: 10.1007/s11207-011-9766-x

Rivera, Y. J., Badman, S. T., Stevens, M. L., et al. 2024, Science, 385, 962, doi: 10.1126/science.adk6953

Rouillard, A. P., Pinto, R. F., Vourlidas, A., et al. 2020, A&A, 642, A2, doi: 10.1051/0004-6361/201935305

Schatten, K. H. 1971, Cosmic Electrodynamics, 2, 232

Schatten, K. H., Wilcox, J. M., & Ness, N. F. 1969, Solar Physics, 6, 442, doi: 10.1007/BF00146478

Schwadron, N. A., & McComas, D. J. 2003, Geophysical Research Letters, 30, doi: https://doi.org/10.1029/2002GL016499

Shi, G., Feng, L., Ying, B., Li, S., & Gan, W. 2024, The Astrophysical Journal, 970, 131, doi: 10.3847/1538-4357/ad5200

Shi, X., Fu, H., Huang, Z., et al. 2024, ApJ, 972, 54, doi: 10.3847/1538-4357/ad5be1

Smith, E. J., & Balogh, A. 1995, Geophys. Res. Lett., 22, 3317, doi: 10.1029/95GL02826

Steyn, P. J., & Burger, R. A. 2020, The Astrophysical Journal, 902, doi: 10.3847/1538-4357/abb2a5

Steyn, P. J., Johnson, D., Botha, G. J. J., & Régnier, S. 2024, ApJ, 966, 77, doi: 10.3847/1538-4357/ad3356

Tian, H., Harra, L., Baker, D., Brooks, D. H., & Xia, L. 2021, SoPh, 296, 47, doi: 10.1007/s11207-021-01792-7

Viall, N. M., & Borovsky, J. E. 2020, Journal of Geophysical Research (Space Physics), 125, e26005, doi: 10.1029/2018JA02600510.1002/essoar.10502606.1

Wang, Y. M., & Sheeley, Jr., N. R. 1992, ApJ, 392, 310, doi: 10.1086/171430

Wilson, III, L. B., Brosius, A. L., Gopalswamy, N., et al. 2021, Reviews of Geophysics, 59, e2020RG000714, doi: 10.1029/2020RG00071410.1002/essoar.10504309.2

Yang, L., Hou, C., Feng, X., et al. 2023, ApJ, 942, 65, doi: 10.3847/1538-4357/aca52d

Yang, L., Feng, X., Shen, F., et al. 2025, ApJ, 981, 109, doi: 10.3847/1538-4357/adb313

Yang, L. P., Feng, X. S., Xiang, C. Q., et al. 2012, J. Geophys. Res., 117, A08110, doi: 10.1029/2011JA017494

Yang, Z., Tian, H., Tomczyk, S., et al. 2024, Science, 386, 76, doi: 10.1126/science.ado2993

Yang, Z., Tian, H., Tomczyk, S., et al. 2020a, Science China Technological Sciences, 63, 2357, doi: https://doi.org/10.1007/s11431-020-1706-9

Yang, Z., Bethge, C., Tian, H., et al. 2020b, Science, 369, 694, doi: 10.1126/science.abb4462

Zhao, X., & Hoeksema, J. T. 1994, Solar Physics, 151, 91, doi: 10.1007/BF00654084

Zhao, X., & Hoeksema, J. T. 1995, Journal of Geophysical Research: Space Physics, 100, 19, doi: 10.1029/94JA02266

Zirker, J. B. 1977, Reviews of Geophysics, 15, 257, doi: https://doi.org/10.1029/RG015i003p00257

Zurbuchen, T. H., Schwadron, N. A., & Fisk, L. A. 1997, Journal of Geophysical Research: Space Physics, 102, 24175, doi: https://doi.org/10.1029/97JA02194